Non-ideal stability analysis of differentially rotating plasmas with global curvature effects

Alexander Haywood*
Department of Electrical and Computer Engineering, Princeton University, Princeton, New Jersey 08544

Fatima Ebrahimi
Princeton Plasma Physics Laboratory, Princeton University, Princeton, New Jersey 08543 and Department of Astrophysical Sciences, Princeton University, Princeton, New Jersey 08544

(Dated: December 3, 2025)

The linear stability of global non-axisymmetric modes in differentially rotating, magnetized, non-ideal plasma is critical to classifying turbulence and transport phenomena. We investigate the competition between the local Magneto-Rotational Instability (MRI) and the Magneto-Curvature Instability (MCI)–a distinct non-axisymmetric low-frequency curvature-driven global branch that appears alongside MRI. To accomplish this, we developed a non-ideal global spectral method, which is validated against NIMROD code simulations. This spectral approach allows for the direct derivation of an extended effective potential formalism and a resistive Alfvénic resonance condition, providing a framework for direct analysis of energy contributions and confinement mechanisms. Our study reveals that the global, low-frequency MCI persists at low magnetic Reynolds numbers (Rm), whereas the localized, high-frequency MRI is stabilized by diffusive broadening of its structure around its Alfvénic resonances. Consequently, we identify the global MCI branch as the primary onset mechanism for non-axisymmetric magnetohydrodynamic instability in systems with finite curvature, e.g., astrophysical rotators. We establish distinct parameter regimes for mode dominance: MCI prevails in geometrically moderate-thickness disks with intermediate curvature and radial gaps, while MRI dominates in thin, low-curvature disks with large radial gaps. Mode competition is also highly sensitive to the flow profile, particularly vorticity and its gradient, with non-uniform shear profiles exhibiting more robust instability due to flow-curvature (i.e. the second derivative of the flow profile) and shear contributions. A key outcome is the development of *spectral diagrams* derived from the global spectral method. These diagrams comprehensively map dominant instabilities and their characteristics, offering a predictive tool for critical onset parameters (i.e., flow curvature, magnetic field, and Rm) and facilitating the interpretation of experimental and simulation results. Notably, these diagrams demonstrate that the global MCI is generally the sole unstable mode at the initial onset of non-axisymmetric instability.

I. INTRODUCTION

Observations [1] and experiments have established that differentially rotating plasmas in the presence of magnetic fields exhibit turbulence-enhanced momentum transport. Compact objects like M87 are theorized to possess large differential flow, global curvature, and strong magnetic fields [2]. These observations highlight the need to study the global drivers of turbulence, especially in the strong-field limit.

Systems exhibiting a weak magnetic field and a differential flow are unstable to magnetohydrodynamic (MHD) perturbations, separately from the traditional hydrodynamic (HD) instability limit–defined as $q(r) = -\frac{r\Omega'}{\Omega} < 2$ for the rotation profile $\Omega(r)$. In the context of accretion flows, the magnetorotational instability (MRI) [3–5] has long been theorized to be the primary driver of this turbulence in hydrodynamically stable flows. In this paper, we extend the stability analysis of differentially rotating systems to account for global spatial and (magnetic and velocity) field curvature effects, which are particularly significant in the context of astrophysical rotators such as accretion disks [6] and stellar interiors, as well as for interpreting laboratory experiments [7–10].

Both global axisymmetric and non-axisymmetric MRI have been investigated thoroughly locally [11–15], globally [7, 16, 17], and experimentally [7–10, 18]. Recent linear and nonlinear studies [10, 19–23] have emphasized the importance of studying non-axisymmetric perturbations. In particular, experiments and simulations uncovered the onset of a low-frequency global non-axisymmetric mode occurring at magnetic Reynolds number lower than expected for ideal Taylor-Couette flows [20]. A global mode with similar characteristics to that observed was recently found in the ideal limit, the magneto-curvature instability (MCI)– the global branch of non-axisymmetric MRI– and was shown to be driven by both spatial and (flow and magnetic) mean-field curvature [19, 23]. Non-axisymmetric global modes were shown to be mostly confined between Alfvénic resonant points (where the Doppler shifted mode frequency is equal to the Alfvén frequency) [24, 25], and could persist at stronger magnetic fields (where axisymmetric MRI modes are stable) [19, 23]. We will demonstrate that the

* ahaywood@princeton.edu

global structure of this mode makes it persistent upon introducing diffusive effects and argue that the onset of non-axisymmetric MHD instability will generally occur at this mode.

This study investigates the stability of rotating plasma disks containing vertical or azimuthal magnetic fields. We employ a combination of techniques: local (WKB) analysis, global spectral analysis, and direct linear initial-value simulations. In particular, our analysis yields the complete modal spectra and all instability branches (including growth rates, frequencies, and Alfvénic resonances) for non-axisymmetric instabilities, which were largely neglected in earlier local and global [26] studies. In this study, *we highlight why global treatment matters and showing that a complete picture of the full instability spectrum requires incorporating both finite system curvature and flow curvature in the stability analysis.* Our investigation yields the following key findings:

1. The Magneto-Curvature Instability (MCI) and Magneto-Rotational Instability (MRI) retain distinct modal characteristics, each exhibiting unique mode structure and frequency, under identical magnetic field strength ($B_0 = V_A/V_0$), wave numbers (m, k), domain, and flow configurations. Although they could partially overlap over some parameter range, each mode defines a separate instability boundary.

2. MRI's localized structure is selectively damped upon introducing diffusive effects. Consequently, the general onset of non-axisymmetric instability (at critical Rm) is expected to occur at the MCI mode (presented in Sections IV D,V A 1, and V B 3).

3. Increased vorticity ($\Gamma = (\nabla \times \mathbf{v})_z = \Omega(2-q)$) (and thus smaller shear) will generally lead to the onset of instability at a lower magnetic Reynolds number (Rm), as it destabilizes both MRI and MCI. Vorticity gradients ($\Gamma' = -(\frac{q(2-q)}{r\Omega} + \Omega q')$) have a more complicated relationship with both modes, and damping/destabilization intrinsically depends on mode frequency and field strength. Moreover, as vorticity is comprised of independent curvature (2Ω) and shear terms ($-q\Omega$), we study the effect of curvature via tuning q. In this paper, we specifically define relative flow curvature as $\langle\Gamma'\rangle_r / \langle\Gamma\rangle_r$ ($\langle.\rangle_r$ the radial average), because this provides a normalized measure of the global competition between shear and curvature across the flow. We demonstrate that larger flow curvature leads to increased instability of the MCI modes, while MRI remains relatively agnostic due to its local nature (presented in Section V B).

4. Regimes with either a turning point in the vorticity profile or a sufficiently deep vorticity well exhibit hydrodynamic (HD) instability, and at finite field, these profiles exhibit hybrid MCI-HD modes, as the MCI mode bifurcates into an HD branch at zero field. These MCI-HD hybrid modes are resonance localized at low magnetic fields. The onset of MHD instability in these regimes can be viewed as a bifurcation process of the Alfvénic resonances about the Corotation point in the flow (see Sec. V B 2).

5. MCI dominates in disks with moderate thickness (moderate vertical aspect ratio, $\Delta z/\Delta r \sim 1$), spatial curvature ($r_2/r_1 \sim O(1)$), and radial aspect ratio (radial gap) $r_1/(r_2 - r_1) < 1$. Similarly, MRI dominates in thin disks ($\Delta z/\Delta r \ll 1$), low spatial curvature ($r_2/r_1 \to \infty$), and small radial aspect ratio (large radial gap) ($r_1/(r_2 - r_1) \to 0$).

We also extend the effective potential formalism and conclude that introducing (fluid and magnetic) diffusive effects causes all modes to become broader with respect to their Alfvénic resonances. This, in turn, leads to an increased stabilizing effect for resonance-localized modes, such as MRI and low-field MCI, unlike global MCI, which exhibits only a single resonance in the domain. With this potential formalism, we also demonstrate that at finite Rm the system loses its time-reversal symmetry. We utilize these observations to conclude that the general onset of MHD instability will occur at the global MCI mode and introduce a method to provide a coarse onset boundary and set of critical onset parameters. In addition, this method provides coarse boundaries of where each unstable mode will be dominant. These boundaries offer rough, experimental domains of where to search for MRI modes and predict that the onset of MRI can be observed as a discontinuous transition in the mode's frequency from low to high as the Magnetic Reynolds number (Rm) is increased.

The paper is structured as follows: Section II describes the physical model and governing equations we utilize. Section III details our first method, a local WKB approximation, which we utilize to obtain a non-ideal dispersion relation describing instability growth rates; we use this method to explore instability characteristics under perturbation of the domain, flow configuration, and the introduction of diffusive effects.

Section IV introduces our global stability analysis method, in which we derive and solve an ordinary differential equation (ODE) that captures the large-scale structure of the instabilities across the disk. This ODE is an extension of the global method derived in [19], which we extend by employing an approximation on the diffusive contributions' structure and validating findings against simulations. We utilize this extended ODE to form an effective potential formalism for the confinement of ideal and non-ideal modes and explore how confining potentials vary with diffusive contributions.

Section V presents results from direct initial-value NIMROD [27, 28] simulations for different magnetic field configurations and compares them with solutions to the

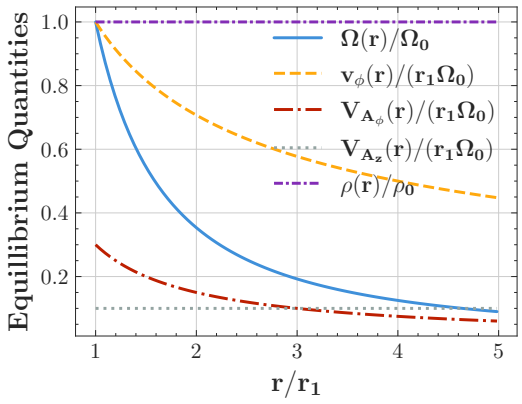

FIG. 1: Variation of normalized equilibrium quantities with radius for an unstratified, currentless Keplerian disk. The magnetic field orientation is chosen such that $V_{A_\phi}(r=0)/(r_1\Omega_0) = 0.3$ and $V_{A_z}(r=0)/(r_1\Omega_0) = 0.1$, which is consistent with past analysis [19].

global ODE to verify our methodologies. Here, we introduce *spectral diagrams* that map out the instability domain for every unstable mode and provide the tools to classify the conditions of MHD onset coarsely. Importantly, this method is able to handle general Prandtl number, magnetic Reynolds number, and mode configuration (general k_z and m). Here, we demonstrate instability domains for small viscosity (Pm$= 10^{-6}$), intermediate viscosity (Pm$= 10^{-1}$), and high viscosity (Pm $= 1$) regimes, while magnetic Reynolds number (Rm) and Alfvén speed (V_A) are varied for low-m modes. We then examine how the variation of flow profile (specifically, the shear parameter $q(r)$, vorticity, and its gradient) affects MRI and MCI, demonstrating that both remain MHD unstable. We also discuss the conditions under which purely hydrodynamic instability arises and how it interacts with the MCI. We establish that in hydrodynamically unstable configurations, the MCI bifurcates into a Corotation localized hydrodynamic mode in the absence of a magnetic field. We similarly demonstrate that hydrodynamic instability can occur for $q(r) < 2$ given sufficiently deep vorticity wells and show that these configurations also exhibit resonance-localized MCI modes. Section V C then explores the impact of changing the disk's overall curvature and shape (ratio of radial and vertical aspect ratios), confirming that current experimental setups likely operate in a regime where the MCI is dominant. Finally, Section VI summarizes our key findings and suggests potential experimental strategies for isolating and observing these different types of instabilities.

II. MODEL

This study focuses on modeling the dynamics of cylindrical plasma disks threaded with vertical or azimuthal magnetic fields. Our investigation utilizes three main approaches with increasing hierarchy: local WKB analysis, global spectral analysis, and linear initial-value simulations. All methods are based on the incompressible, resistive Magnetohydrodynamics (MHD) equations,

$$\rho\left(\frac{\partial}{\partial t} + \mathbf{v}\cdot\nabla\right)\mathbf{v} = \frac{(\mathbf{B}\cdot\nabla)\mathbf{B}}{\mu_0} - \nabla\left(p + \frac{B^2}{2\mu_0}\right) + \rho\nu\nabla^2\mathbf{v} \tag{1}$$

$$\frac{\partial \mathbf{B}}{\partial t} = \nabla\times(\mathbf{v}\times\mathbf{B}) - \eta\nabla^2\mathbf{B} \tag{2}$$

where $\mathbf{v}$, $\mathbf{B}$, p, μ_0, ρ, η, and ν are the fluid velocity, magnetic field, pressure, magnetic permeability, density, magnetic, and viscous diffusivities, respectively. Furthermore, incompressibility ($\nabla\cdot\mathbf{v} = 0$), the divergence free condition ($\nabla\cdot\mathbf{B} = 0$), and a spatially uniform density are assumed ($\rho(r) = \rho$).

First, in Section III, we begin by performing a local WKB expansion on mean fields $\mathbf{v}_0 = r\Omega(r)\hat{\phi}$, $\mathbf{B}_0 = B_\phi\hat{\phi} + B_z\hat{z}$ and obtain a complete diffusive dispersion relation.

Second, we perform a global linear perturbative analysis and derive a second-order ordinary differential equation (ODE) governing the dynamics of the instabilities. We utilize shooting to obtain both eigenmodes and eigenvalues of the instabilities. We recast the ODE via an integrating factor transform to obtain an extended effective potential formalism [23], utilizing eigenvalues from shooting to obtain confining potentials. We explore scaling and structure of these modes/potentials with resistivity, flow, and domain configuration in Sections V, V B, V C respectively. Our analyses consider ten explicit flow configurations and three radial aspect ratios. We perturb flow configurations to classify the scaling of MHD modes with different relative vorticity, vorticity gradients, flow curvature, and the presence of hydrodynamic instability. All linear simulations are run with the Keplerian profile; however, we simulate all explicit radial aspect ratios. Unlike the study by [19], which involved a changing relative disk shape ($\Delta z/\Delta r$), our work investigates radial aspect ratio scaling using both direct numerical simulations with a fixed disk shape ($\Delta z/\Delta r = 2$) and spectral methods that vary the radial and vertical radial aspect ratios independently. Moreover, this choice of fixed disk shape follows from [19] and allows for direct comparison to previous work; this also results in our frequent use of the vertical wavenumber $r_1k_1 = \pi/4$ ($k_z = nk_1,\ r_1k_1 = 2\pi/\Delta z$).

Third, we perform direct linear initial-value simulations using the NIMROD code (Non-Ideal Magnetohydrodynamics with Rotation, an Open Discussion project) [27]. NIMROD solves the time-dependent MHD equations numerically using a high-order finite element mesh for the poloidal plane (r-z). Meanwhile, it is pseudo-spectral in the periodic (ϕ) direction with Fast Fourier Transforms (FFTs) (quantized by m). Although NIMROD can simulate complex non-linear physics, here we

use it to model only the growth of the non-axisymmetric ($m = 1$) modes from small random initial noise. Simulations begin from an equilibrium state (e.g., Keplerian flow with uniform vertical or azimuthal field) and track the evolution of the single mode (m=1) non-axisymmetric perturbations. The radial boundaries are treated as solid, conducting walls, while the vertical and azimuthal directions are periodic. The numerical accuracy of these simulations is verified by varying mesh resolution and simulation time step. The parameters and geometries tested are detailed in Table I and Figure 9. Comparing the simulation results with the global ODE methods allows us to validate our models and classify the stability in different configurations. However, understanding the combined effect of multiple coexisting modes on accretion would require future non-linear simulations.

III. LOCAL STABILITY METHODS

We begin by employing a WKB approximation to study the local dynamics of linear perturbations about mean fields $\mathbf{v}_0 = r\Omega(r)\hat{\phi}$ and $\mathbf{B}_0 = B_\phi(r)\hat{\phi} + B_z\hat{z}$. We apply this approximation to the linearized MHD equations (Eqns. 1, 2) assuming perturbations take a wave-like form $\boldsymbol{\xi} = \boldsymbol{\xi}_0 e^{i(\mathbf{k}\cdot\mathbf{r}-\omega t)}$. Here $\mathbf{k}$ is the wave-vector with components k_r, $k_\phi = m/r$, and k_z representing variations in the radial, azimuthal, and vertical directions, respectively (with m being the azimuthal mode number). Meanwhile, the complex frequency $\omega = \omega_r + i\gamma$ contains the mode's frequency (ω_r) and growth rate (γ). By further assuming the plasma is incompressible, these perturbed quantities can be represented in the matrix equation $\mathbf{M}\boldsymbol{\chi} = 0$ (Eq. 3), where $\boldsymbol{\chi}$ contains the perturbed velocity and magnetic field components.

$$\mathbf{M}\boldsymbol{\chi} = \begin{bmatrix} i\bar{\omega} - \eta\bar{k}^2 & -\frac{2ik_\phi\eta\delta_c}{r} & iF & 0 \\ \frac{\partial\Omega}{\partial \ln r} + \frac{2ik_\phi\eta\delta_c}{r} & i\bar{\omega} - \eta\bar{k}^2 & \frac{2B_\phi}{r}\delta_c & iF \\ \frac{iF}{\mu_0\rho}\left(1 - \frac{\bar{k}_r k_r}{k_z^2}\right) & \frac{1}{\mu_0\rho}\left(iF\frac{k_r k_\phi}{k_z^2} - \frac{B_\phi}{r}\delta_c\right) & i\bar{\omega}\left(1 - \frac{\bar{k}_r k_r}{k_z^2}\right) - \nu\bar{k}^2 & 2\Omega + \frac{i\bar{\omega}k_r k_\phi}{k_z^2} - \frac{2ik_\phi\nu\delta_c}{r} \\ \frac{iF}{\mu_0\rho}\frac{\bar{k}_r k_\phi}{k_z^2} & \frac{iF}{\mu_0\rho}\left(1 + \frac{k_\phi^2}{k_z^2}\right) & i\bar{\omega}\frac{\bar{k}_r k_\phi}{k_z^2} - \frac{\kappa^2}{2\Omega} + \frac{2ik_\phi\nu\delta_c}{r} & i\bar{\omega}\left(1 + \frac{k_\phi^2}{k_z^2}\right) - \nu\bar{k}^2 \end{bmatrix} \begin{bmatrix} \tilde{B}_r \\ \tilde{B}_\phi \\ \tilde{V}_r \\ \tilde{V}_\phi \end{bmatrix} = 0 \quad (3)$$

where $F = \mathbf{k}\cdot\mathbf{B}_0 = k_\phi B_\phi + k_z B_z$, $k_\phi = m/r$. Meanwhile, $\bar{\omega} = \omega - m\Omega$ and $\kappa^2 = 4\Omega^2 + \frac{d\Omega^2}{d\ln r}$ are the Doppler shifted and epicyclic frequencies respectively. Meanwhile, we define $k^2 = \bar{k}_r k_r + k_\phi^2 + k_z^2$, with $\bar{k}_r = k_r - \frac{i\delta_c}{r}$ and $\bar{k}^2 = k^2 + \frac{\delta_c}{r^2}$, with δ_c arising due to the cylindrical geometry's finite curvature. Finally, the current-free condition mandates that $\frac{\partial B_\phi}{\partial r} = -B_\phi/r$.

The requirement for a non-trivial solution (i.e., for an instability to exist) is that the determinant of the matrix $\mathbf{M}$ must be zero. This condition yields a fourth-order polynomial equation (Eq. 4) known as the local dispersion relation.

$$\bar{\omega}^4 + C_3\bar{\omega}^3 + C_2\bar{\omega}^2 + C_1\bar{\omega} + C_0 = 0 \quad (4)$$

with coefficients C_3, C_2, C_1, and C_0 defined in Appendix A Moreover, for later use we will define the Alfvén frequency $\omega_A = \frac{F}{\sqrt{\mu_0\rho}}$ and $\omega_c = \frac{2B_\phi}{r\sqrt{\mu_0\rho}}$.

In a real disk, k_z and m are quantized by the disk's boundaries. We define the profile of the disk in the $r-\phi$ plane via r_1, r_2, z_1, z_2. r_1 and r_2 define the radial boundaries of the disk and are the inner and outer radius, respectively. Similarly, z_1 and z_2 define the vertical boundaries and are the lower and upper surface, respectively (see Fig. 9 for a visualization). We then define wave numbers $k_r = 2\pi l/(r_2 - r_1)$ and $k_z = 2\pi n/(z_2 - z_1)$ where n, l are positive integers. To compare with later results, we use the inner radius (r_1) and the rotation frequency at the inner wall ($\Omega(r_1) = \Omega_0$) to define dimensionless numbers: the magnetic Prandtl number $\mathrm{Pm} = \nu/\eta$, the magnetic Reynolds number $\mathrm{Rm} = r_1^2\Omega_0/\eta$, and the Lehnert number $B_0 = V_A/(r_1\Omega_0)$. All radially varying quantities (Ω, ω_A, etc) are evaluated at the inner boundary for this local analysis.

We first study the dispersion relation with a standard Keplerian profile ($\Omega(r) \propto 1/r^{3/2}$) and a purely vertical magnetic field, with results shown in Figure 2. In the ideal case (no diffusion, $\eta = \nu = 0$, panels a-c), the dominant instabilities (largest γ) exhibit small vertical wavelengths (high k_z), large radial wavelengths (low k_r), and are strongly non-axisymmetric. However, in the presence of significant diffusion (high η, ν, corresponding to low Rm given Pm = 1 in panels d-f), the dominant mode shifts towards large vertical and radial wavelengths (low k_z and k_r) yet remains distinctly non-axisymmetric. Thus, introducing diffusivity leads to increased globality in the structure of the dominant instabilities. Consequently, motivated by recent simulations and experiments that observed such modes at low Rm, this paper will focus primarily on the $m = 1$ non-axisymmetric modes.

We also examined how the flow configuration affects instabilities by considering three additional power-law profiles ($\Omega(r) \propto 1/r^q$ with $q = 5/4, 7/4, 2$) shown in Figure 3. Across all profiles, low Rm dominant instabilities are characterized by large-scale global (low k_r, k_z) non-axisymmetric ($m = 1$) structure. Figure 3 demonstrates explicitly how the growth rate depends on the magnetic field strength (V_A) and magnetic Reynolds number (Rm) for the most global modes ($m = 1$, $r_1 k_z = 1$, $r_1 k_r = 0$)

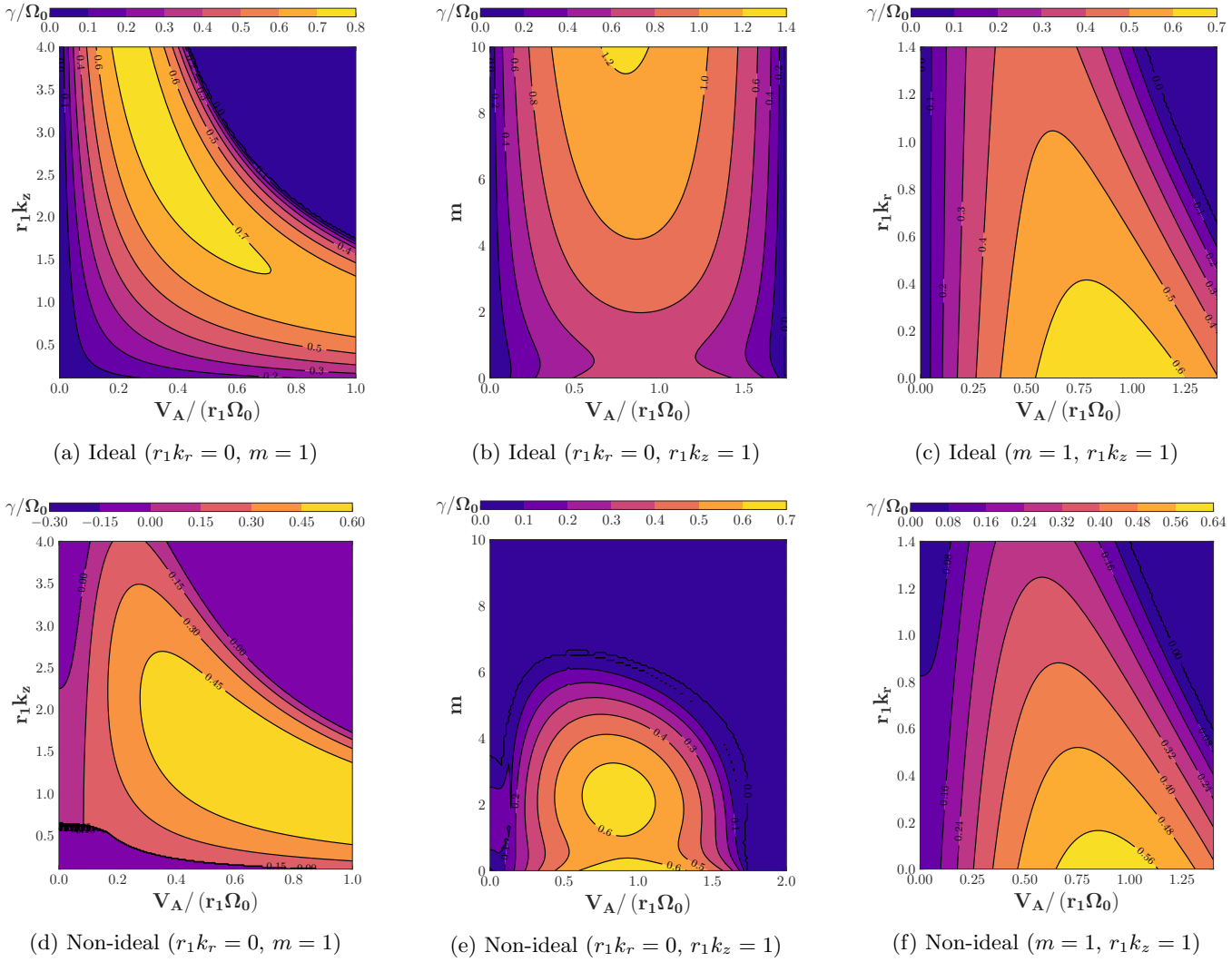

(a) Ideal ($r_1 k_r = 0$, $m = 1$)

(b) Ideal ($r_1 k_r = 0$, $r_1 k_z = 1$)

(c) Ideal ($m = 1$, $r_1 k_z = 1$)

(d) Non-ideal ($r_1 k_r = 0$, $m = 1$)

(e) Non-ideal ($r_1 k_r = 0$, $r_1 k_z = 1$)

(f) Non-ideal ($m = 1$, $r_1 k_z = 1$)

FIG. 2: Growth rate contours from local dispersion relation (Eq. 4) under a vertical magnetic field and Keplerian flow profile. The top panel (a,b,c) all consider variation of disk configuration without non-ideal effects (Rm $= \infty$, no viscosity), meanwhile the bottom panel (d,e,f) consider the same variation with diffusive effects (Pm $= 1$ and Rm $= 31$). In (a) and (d), the vertical radial aspect ratio is varied, whereas (c) and (f) vary the radial aspect ratio. Meanwhile, in (b,e), we vary the azimuthal mode number (m). This demonstrates that the most unstable modes under heavy diffusion are non-axisymmetric modes ($m \neq 0$) and global (low k_r and k_z). All radial quantities are evaluated at the inner boundary (r_1), and exhibit curvature effects ($\delta_c = 1$).

among different flow configurations. A key finding is that the conditions required for the onset of instability (the minimum field strength and Rm) strongly depend on the flow profile. Specifically, flow configurations with larger shear (larger q) become unstable at lower Rm (cf. Figs. 3a,b,c,d). We will later demonstrate that that the reverse is true in the global consideration, (see Sec. V B 1) by studying the free energy contributions.

This difference is a key manifestation of the limitations of the WKB method: it assumes that background configurations are uniform locally, whereas in a real disk, properties like the velocity ($v_\phi = r\Omega(r)$) and the magnetic field strength are intrinsically radially-dependent (as shown in Figure 1). The radial dependence of these background quantities, therefore, renders the definition of a radial wave number ill-posed. As such, the WKB results should indicate rough scaling behavior rather than being quantitatively precise for the whole disk, and should indicate the importance of studying specific quantities. To perform a more accurate and comprehensive analysis that accounts for these radial variations, we need to employ global methods that explicitly solve for the instability structure across the entire radial extent of the disk.

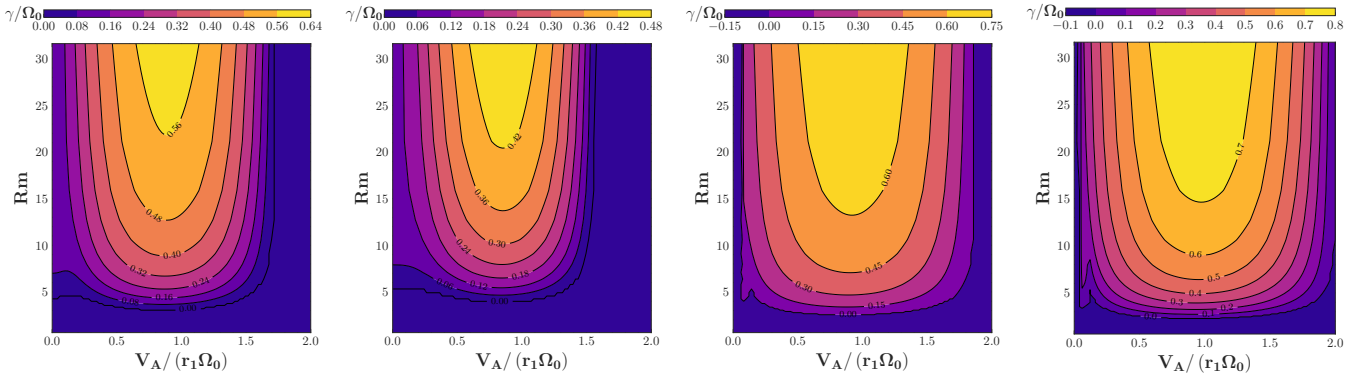

(a) Keplerian ($q = 3/2$) (b) $q = 5/4$ (c) $q = 7/4$ (d) $q = 2$

FIG. 3: Growth rate contours from local dispersion relation (Eq. 4) for global non-axisymmetric modes ($m = 1$, $r_1 k_r = 0$, $r_1 k_z = 1$, $\delta_c = 1$) under a vertical magnetic field as flow profile is varied. We consider four discrete power-law profiles ($\Omega(r)/\Omega_0 = 1/r^q$): Keplerian ($q = 3/2$) (a), $q = 5/4$ (b), $q = 7/4$ (c), and $q = 2$ (d). Flow configuration changes the domain over which the modes are unstable at finite Rm and the critical Rm and magnetic field for the onset of instability. All radial quantities were evaluated at the inner boundary.

IV. NON-IDEAL GLOBAL STABILITY METHODS

Moving beyond the local WKB analysis, we develop a global model that accounts for radial variations across the disk. Our approach extends the ideal MHD framework developed by [19] to include the effects of finite resistivity and viscosity (corresponding to finite and non-zero Rm and/or Pm). Core to this development is the derivation of a one-dimensional Ordinary Differential Equation (ODE) that governs the radial structure of linear instabilities. To keep the ODE tractable and non-coupled, we employ an approximation targeting only the diffusive contributions (the last two terms on the RHS of Eqns. 1, 2), an approach first proposed by [29]. This method requires the definition of a pseudo-radial wave-vector for the diffusive contributions, and we propose two candidate approximations. We term the approximations "MWKB" (modified WKB-like) and"TWKB" (traditional WKB-like) and test them by comparing to direct numerical simulations using NIMROD (details in Sec. IV A).

Once the extended ODE is established, we solve it numerically using the shooting method to find the instability properties: the eigenvalues (ω), which represent the complex frequencies (frequency $\mathrm{Re}(\omega) = \omega_r$ and growth rate $\mathrm{Im}(\omega) = \gamma$), and the corresponding eigenfunctions, which describe the radial structure of the instability. This approximation global model allows us to:

1. Identify unstable modes and map how different families (or "branches") of solutions change as flow/field/disk configuration and Rm/Pm/B_0 are varied (Sec. IV B).

2. Define locations of Alfvénic resonances in the presence of diffusion–points in the regime where the Doppler shifted frequency equals the Alfvén frequency. These resonances are critical to describing the mode structure of instabilities and confinement mechanisms (Sec. IV C).

3. Extend the effective potential formalism, previously used in the ideal MHD regime [23], to the non-ideal regime to analyze how diffusion affects the confinement and stability of non-axisymmetric modes (Sec. IV D).

Our global analysis method consider small linear perturbations about the same equilibrium state as before: a differentially rotating flow $\mathbf{v}_0 = r\Omega(r)\hat{\phi}$ and a magnetic field $\mathbf{B}_0 = B_\phi(r)\hat{\phi} + B_z\hat{z}$. Unlike the WKB method, we now allow the radial structure of perturbations to vary arbitrarily across the disk. We assume these perturbations are wave-like in the azimuthal (ϕ) and vertical (z) directions, oscillating with complex frequency $\omega = \omega_r + i\gamma$. Thus, any perturbed quantity (like velocity $\tilde{\mathbf{v}}$, magnetic field $\tilde{\mathbf{B}}$ or pressure $\tilde{P}$) takes the form $a(r)\exp\left(i\left(m\phi + k_z z - \omega t\right)\right)$. The radial profile $a(r)$ is determined by the dynamics for the given quantity, with the only constraint being that the perturbations vanish at the inner and outer radial boundaries. It's worth noting in the ideal limit ($\eta, \nu = 0$), the displacement vector ($\boldsymbol{\xi}$) [30] can be introduced to decouple $\tilde{\mathbf{v}}$ and $\tilde{\mathbf{B}}$ as the magnetic field is "frozen" in the moving fluid. Given finite viscosity and resistivity, such a method cannot be taken, as the magnetic field lines can now diffuse across fluid elements.

Including the full effects of resistivity and viscosity directly into the global perturbation equations leads to a very complex, high-order differential equation system, making it difficult to solve and interpret physically. To simplify this while retaining the essential physics of diffusion, we adopt an approximation strategy proposed by [29] that targets solely the diffusive terms (viscos-

ity $\propto \nabla^2\mathbf{v}$ and resistivity $\propto \nabla^2\mathbf{B}$). If these diffusive contributions are assumed to be wave-like with radial wavenumber $k_r(r)$, which we need to specify (see Sec. IV A, then leading order diffusive contributions in the short-wave limit can be simplified by the expression $-\nabla^2 \approx k_r^2(r) + m^2/r^2 + k_z^2$. This short-wave condition can be expressed via the radial wavenumber as $|\langle k_r(r)\rangle_r|(r_2 - r_1) \gg 1$ for r_1, r_2 the boundaries of the domain and $\langle . \rangle_r$ the radial average. Considering global variation of perturbed quantities, we utilize $r_2 - r_1$ as the characteristic length instead of r_1. Crucially, this approximation only modifies the diffusive contributions, leaving the ideal dynamics unchanged, and does not presuppose the actual global structure of the instability. Although the approximation was derived in the short-wave limit, their implementations take into account scale-dependent damping (see Sec. IV A). Thus the closure captures how dissipation scales with system system, even for large-scale (global, long-wavelength) modes. This simplification allows us to reduce the governing equations to a second-order one-dimensional ODE.

Applying this diffusive approximation to the viscous and resistive terms in the linearized MHD equations (Eqns. 1-2) leads to a system that can be written in matrix form as $\mathbf{M}\tilde{\boldsymbol{\xi}} = 0$ for $\tilde{\boldsymbol{\xi}} = \left(\tilde{v}_r, \tilde{v}_\phi, \tilde{v}_z, \tilde{B}_r, \tilde{B}_\phi, \tilde{B}_z, \tilde{p}\right)$ and $\mathbf{M}$,

$$\mathbf{M} = \begin{pmatrix} -i\bar{\omega}_\nu & -2\Omega & 0 & -\frac{iF}{\rho\mu_0} & \frac{2B_\phi}{r\rho\mu_0} & 0 & \frac{1}{\rho}\frac{d}{dr} \\ \frac{1}{r}\frac{d}{dr}\left(r^2\Omega\right) & -i\bar{\omega}_\nu & 0 & 0 & -\frac{iF}{\rho\mu_0} & 0 & \frac{im}{r\rho} \\ 0 & 0 & -i\bar{\omega}_\nu & 0 & 0 & -\frac{iF}{\rho\mu_0} & \frac{ik_z}{\rho} \\ -iF & 0 & 0 & -i\bar{\omega}_\eta & 0 & 0 & 0 \\ -\frac{2B_\phi}{r} & -iF & 0 & -r\frac{d\Omega}{dr} & -i\bar{\omega}_\eta & 0 & 0 \\ 0 & 0 & -iF & 0 & 0 & -i\bar{\omega}_\eta & 0 \\ \frac{1}{r} + \frac{d}{dr} & \frac{im}{r} & ik_z & 0 & 0 & 0 & 0 \\ 0 & 0 & 0 & \frac{1}{r} + \frac{d}{dr} & \frac{im}{r} & ik_z & 0 \end{pmatrix} \tag{5}$$

where $F = \boldsymbol{k}\cdot\boldsymbol{B}_0 = \frac{mB_\phi}{r} + k_z B_z$, and $\bar{\omega}_{\eta,\nu} = \bar{\omega} - i(\eta,\nu)\cdot\left(k_r^2(r) + \frac{m^2}{r^2} + k_z^2\right)$. Moreover, the current free condition has been imposed ($-\frac{\partial B_\phi}{\partial r} = B_\phi/r$). This system can be algebraically reduced to a single second-order ODE for the radial structure of instabilities, which we write in terms of the variable $\xi_r = -r\tilde{v}_r/(i\bar{\omega}_\eta)$:

$$\frac{d}{dr}\left(f\frac{d\xi_r}{dr}\right) + s\frac{d\xi_r}{dr} - g\xi_r = 0 \tag{6}$$

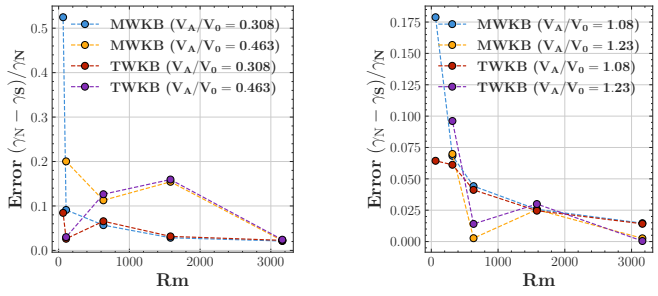

(a) (b)

FIG. 4: Growth rate error between resistive global shooting method (γ_S) and NIMROD simulations (γ_N) for fixed magnetic field slices. We utilize the MCI $1k_1$ ($r_1k_1 = \pi/4$) mode for testing, as it is the only fixed k_z mode with a large enough domain of instability to test a range of magnetic Reynolds numbers. In (a) and (b) we compare vertical and azimuthal field errors between the "MWKB" and "TWKB" approximations, respectively.

where the coefficients f, s, and g are defined as,

$$f = \frac{r\left(\omega_A^2 - \bar{\omega}_\nu\bar{\omega}_\eta\right)}{k_z^2r^2 + m^2}, \quad s = \frac{m(\bar{\omega}_\nu - \bar{\omega}_\eta)}{k_z^2r^2 + m^2}r\Omega',$$

$$g = \frac{\mathrm{d}}{\mathrm{dr}}\left\{\frac{m}{(k_z^2r^2 + m^2)}\left[(\bar{\omega}_\eta - \bar{\omega}_\nu)\,r\Omega' + (2\Omega\bar{\omega}_\eta + \omega_A\omega_c)\right]\right\}$$
$$+\frac{\left(\omega_A^2 + \omega_c^2 - \bar{\omega}_\nu\bar{\omega}_\eta\right)}{r} + \frac{\omega_s^2}{r}\left(\frac{\omega_A^2 - \frac{k_z^2r^2\bar{\omega}_\eta^2 + m^2\bar{\omega}_\eta\bar{\omega}_\nu}{k_z^2r^2+m^2}}{\omega_A^2 - \bar{\omega}_\nu\bar{\omega}_\eta}\right)$$
$$-\frac{k_z^2r}{k_z^2r^2 + m^2}\frac{\left(2\Omega\bar{\omega}_\eta + \omega_A\omega_c\right)^2}{\omega_A^2 - \bar{\omega}_\nu\bar{\omega}_\eta} + \frac{k_z^2r^2\left(\bar{\omega}_\eta - \bar{\omega}_\nu\right)}{k_z^2r^2 + m^2}\frac{\omega_A\omega_c\Omega'}{\omega_A^2 - \bar{\omega}_\nu\bar{\omega}_\eta} \tag{7}$$

and the coefficients ω_A and ω_c are defined as,

$$\omega_A = \frac{F}{\sqrt{\rho\mu_0}} = \frac{\mathbf{k}\cdot\mathbf{B}_0}{\sqrt{\rho\mu_0}},\ \omega_c = \frac{2B_\phi}{r\sqrt{\rho\mu_0}} \tag{8}$$

This ODE matches the results of [29] upon transform of variables, and matches previously derived ideal MHD results [19] (see Sec. B). In the following section, (Sec. IV A), we will discuss how effective wave-vectors are utilized to model this ODE's diffusive contributions. Then, in Section IV B, we will discuss how we obtain global solutions to this ODE and analyze these solutions compared to NIMROD simulations in Section V.

A. Choosing $k_r^2(r)$

A crucial input to the non-ideal ODE (Eq. 6) is the choice of the effective radial wavenumber $k_r(r)$, used in the diffusive approximation. This choice dictates how the radial scale of diffusion is represented. Since we are modeling global modes, we expect this parameter to depend

on the radii of the domain (r_1, r_2) and/or the radial aspect ratio $r_1/(r_2 - r_1)$. We test two primary candidates:

1. MWKB (Modified WKB-like): $k_r^2(r) = \left(\frac{r_1}{r_2 - r_1}\right) \times \frac{4\pi^2}{r^2}$. This form incorporates a linear dependence on the radial aspect ratio and power law envelope. We developed this method based on the previous suggestion by [29] (scaling with radial aspect ratio squared), which did not accurately capture the growth rates across different simulated geometries (AR0, AR1, AR2). We found, however, that a method that scales linearly with radial aspect ratio, and is multiplied by a WKB-like contribution, was able to reproduce this scaling, with this WKB-like contribution taking the form $(2\pi/r)^2$, instead of $(2\pi/(r_2 - r_1))^2$.

2. TWKB (Traditional WKB-like): $k_r^2(r) = \left(\frac{\pi}{r_2 - r_1}\right)^2 - i\left(\frac{\pi}{r_2 - r_1}\right)/r$. This form arises from applying a standard WKB method to the Laplacian operator in cylindrical coordinates, representing the lowest radial mode number. Importantly, this form introduces an imaginary component related to the curvature of the domain.

We benchmarked these two approximations against direct linear simulations using the NIMROD code, comparing the spectral growth rates (γ_S from shooting vs. γ_N from NIMROD) as shown in Figure 4. Generally, both methods perform better for purely azimuthal magnetic fields, often yielding errors below 20% even at low Rm (see Fig. 4b). For vertical fields, the MWKB approximation shows significantly lower error across much of the test regime, while the TWKB approximation becomes more accurate as Rm $\to 0$. Both methods can reproduce the general scaling under the introduction of diffusive contributions.

While the MWKB/TWKB approximations originate from a short-wave expansion of the Laplacian, they act only through the diffusive terms, effectively parameterizing damping across the domain. The global nature of this model ensures that diffusion is intrinsically mode-dependent, as seen in the selective damping of Alfvén-resonance localized modes (MRI, see Sec. IV D). These approximations prescribe only the local behavior of diffusion, while the dominant contribution is controlled by the characteristic scale of the mode. Benchmarking against NIMROD (Figs. 4, 11) demonstrates this empirical accuracy, so we treat them as effective closures rather than strict asymptotic limits.

The domains of accuracy of each approximation can be quantified by the short-wave condition ($\left|\langle k_r \rangle_r\right| (r_2 - r_1) \gg 1$). The TWKB approximation, rooted in the WKB limit, is expected to be most accurate in the limit $r_2/r_1 \to 1$, and we find this satisfies the short-wave condition. Conversely, we find that the MWKB approximation is better suited for large disks ($r_2/r_1 \gg 1$), and thus both approximations are essential to consider. While finding an optimal $k_r(r)$ that can represent the scaling of diffusion contributions in both limits remains an open question, both MWKB and TWKB approximations provide inexpensive methods to reproduce mode properties (frequencies, growth rates) and structures that correlate well with simulation observables. Further systematic simulations varying r_2/r_1 and z_2/r_1 could help refine the optimal form of $k_r(r)$. This remains a path of future research.

B. Global solutions at finite Rm

We solve the boundary-value ODE (Eq. 6) using the shooting method. For a given guess of the complex frequency ω, we integrate the ODE from the inner boundary (r_1) to the outer boundary (r_2). An eigenfunction exists if and only if the calculated structure satisfies the boundary condition $\xi(r_2) = 0$. Numerically, we search for values $\omega = \omega_r + i\gamma$ where both the real and imaginary components of $\xi_r(r_2)$ (the "tails") are simultaneously zero. Plotting these zero-crossings in the complex ω plane reveals the eigenvalues under specified parameters, as illustrated in Figure 5. This figure also demonstrates how diffusion can eliminate certain solution branches present in the ideal limit.

Typically, the solutions fall into two distinct branches of modes: one associated with low frequencies and large radial scales (which we identify as the Magneto-Curvature Instability, MCI) and another with higher frequencies and more localized structures (identified as the Magneto-Rotational Instability, MRI). The exact frequencies, growth rates, and structure depend on system parameters (magnetic field configuration and strength, m, k_z, Rm, Pm, flow profile, etc). Our analysis generally focuses on the mode with the largest growth rate (γ) on each branch, which is most likely to be observed via experiments and simulations.

An important effect of diffusion becomes apparent when comparing the ideal (Rm $= \infty$ (no viscosity), Fig. 5a) and the non-ideal (finite Rm, Fig. 5b) scans. In the ideal limit, the equations posses time-reversal symmetry, meaning every growth mode ($\gamma > 0$) has a corresponding decaying mode ($\gamma < 0$) with the same frequency (ω_r). Diffusion breaks this symmetry. Furthermore, as we will explore using the effective potential (Sec. IV D), diffusion tends to damp localized modes (like MRI) at a higher rate than global modes (like MCI). This differential damping is evident in the eigenvalues scans (Fig. 5b), where the MRI branch is suppressed at low Rm and the MCI remains unstable. Consequently, MCI (from the low-frequency branch) remains the only unstable mode at sufficiently low Rm.

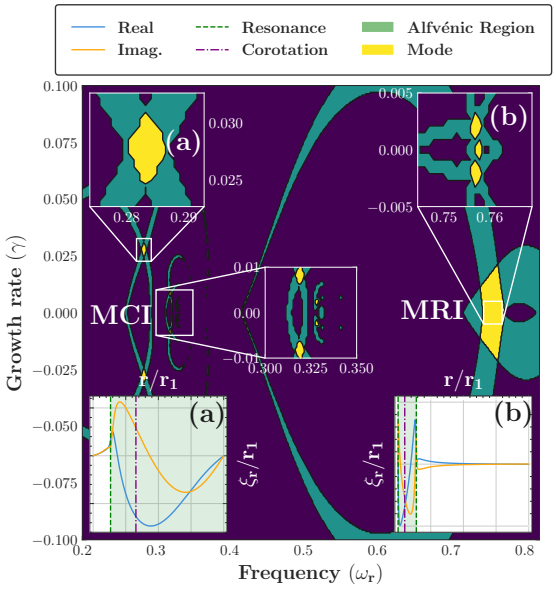

(a)

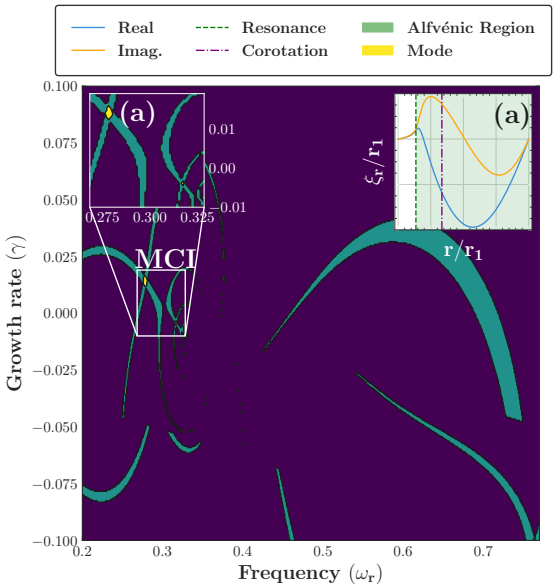

(b)

FIG. 5: MCI vs MRI: Locations of real and imaginary shooting tails and their overlap, which indicates a solution exists fitting the boundary conditions; Purple indicates neither the real nor the imaginary tail is within tolerance of zero; Teal indicates one tail is within tolerance; Yellow indicates both tails are within tolerance of zero, and there exists a solution. Shooting simulation ran for the solely vertical magnetic field of $V_A/(r_1\Omega_0) = 0.308$, $m = 1$, $k_z = 1k_1$ ($r_1k_1 = \pi/4$), and $r_1/(r_2 - r_1) = 1/4$ (AR1) for $\mathrm{Rm} = \infty$ (no viscosity) (a) and $\mathrm{Rm} = 105$ ($\mathrm{Pm} = 1$) (b). The left-hand set of solutions represents the low-frequency curvature mode (MCI), whereas the right-hand set of solutions represents the high-frequency mode (MRI). At high resistivities (panel b), only the low-frequency and global MCI mode remains unstable.

C. Resistive resonance condition

A key concept for understanding mode structure and confinement is the Alfvénic resonance. In the presence of diffusion, these resonances occur at radial locations where the real part of the diffusion-modified Doppler-shifted frequency matches the Alfvén frequency:

$$\mathrm{Re}\left[\omega_A^2 - \bar{\omega}_\eta \bar{\omega}_\nu\right] = 0 \tag{9}$$

These resonance points appear as finite singularities in that ODE formalism (Eq. 6) for any growing/decaying mode ($\gamma \neq 0$). In the effective potential formalism, these resonances manifest as potential barriers [23] and will be further explored given diffusive effects in Section IV D. This definition generalizes the ideal resonance condition ($\bar{\omega} = \pm\omega_A$) and is consistent with previous work in the appropriate limits [19, 24].

Expanding this condition (Eq. 9) reveals how the resonance location depends on the mode's frequency (ω_r), the flow configuration ($\Omega(r)$), the Alfvén frequency, the diffusivities (η, ν), and the total wavenumber ($Q = k_r^2(r) + m^2/r^2 + k_z^2$).

$$\omega_r - m\Omega(r) = \mathrm{Re}\left[\frac{i\,(\eta+\nu)\,Q}{2} \pm \sqrt{\omega_A^2 - \frac{1}{4}\,(\eta-\nu)^2\,Q^2}\right] \tag{10}$$

We have omitted the imaginary components, yet kept $i\,(\eta+\nu)\,Q$ as it is possible that $Q \in \mathbb{C}$ (see the TWKB approximation in Section IV A) and thus contributes to the resonance condition. The presence of diffusion (η, ν) shifts the resonance locations compared to the ideal case. The details of this shift depend on the relative magnitude of viscous to resistive diffusivities (Pm). Nonetheless, we will demonstrate via the effective potential formalism that diffusion generally acts to broaden potential barriers, contributing to the stabilization of modes.

D. Resistive effective potential formalism

To gain deeper physical insight into mode confinement and the sources of free energy, we adapt the effective potential formalism, previously applied in ideal MHD [23, 31, 32], to our non-ideal global ODE (Eq. 6). By applying an integrating factor transform ($\xi_r(r^2) = u(r^2)\Psi(r^2)$ with $u(r^2) = \exp\left[-\frac{1}{2}\int dr^2 \left(\frac{f' + \frac{s}{2r}}{f} + \frac{1}{2r^2}\right)\right]$), we recast the second-order ODE into a Schrödinger-like equation:

$$\Psi''(r^2) - U(r^2, \mathrm{mode})\Psi(r^2) = 0, \tag{11}$$

with,

$$U(r^2, \mathrm{mode}) = \frac{g}{4r^2 f} + \frac{1}{2}\left(\frac{f' + \frac{rs+f}{2r^2}}{f}\right)' + \frac{1}{4}\left(\frac{f' + \frac{rs+f}{2r^2}}{f}\right)^2 \tag{12}$$

Here, Ψ represents the transformed radial mode structure, and $U(r^2, \text{mode})$ is the complex effective potential. This potential U depends on the original ODE coefficients (f, s, g) and thus on all physics parameters of the system, including the mode's complex frequency ω (which must be an eigenvalue found via shooting). We denote this dependence through the acronym "mode" in the definition of the potential.

This formalism allows us to visualize how modes are spatially confined. Regions where $\mathrm{Re}(U)$ is large and positive act as barriers, while regions where $\mathrm{Re}(U)$ is negative act as potential wells where the mode amplitude (Ψ) becomes large. Figure 6 illustrates these potentials for typical MCI and MRI modes with and without diffusive effects. A key observation is that finite diffusion $(\eta, \nu \neq 0)$ tends to smooth out and broaden the potential wells, particularly about the Alfvénic resonances. This broadening makes the modes less tightly confined (more global) than their ideal counterparts, corroborating findings from the local analysis but now linking the structural change explicitly to the resonances. We expect MRI's inherent locality and resonance-localized nature to make the mode's instability more sensitive to diffusive contributions than the inherently global MCI modes.

Comparing the potentials and growth rates for MCI and MRI modes (e.g., Fig. 6 and Fig. 7) reinforces the idea that diffusion affects these modes differently. Figure 7 shows how the growth rates (γ, normalized by the ideal growth rate γ_∞) decrease as diffusion effects increase (Rm decreases) over all magnetic fields where the mode is unstable. The MCI modes retain a larger fraction of their ideal growth rates than MRI at the same Rm. This ultimately results in MCI modes remaining unstable at high diffusivities (lower Rm) than MRI modes, as shown by the magnetic field averaged scalings for MRI and MCI in Figure 7. This difference in scaling with diffusion strongly suggests that the first instability to appear (also known as the onset of instability) will generally be a global MCI mode, likely the one with the smallest vertical wavelength ($k_z = 1k_1$), since diffusion scales with k_z^2.

1. *Energy Criterion*

The effective potential $U(r^2, \text{mode})$ provides insights not only into spatial confinement but also into mode stability (γ). Examining the potential structure for known eigenvalues ω (found via shooting) helps understand these aspects (see Figure 8). In the ideal case, due to time reversal symmetry, the potential for a decaying mode is the complex conjugate of the potential for a growing mode $(U(r^2, \omega) = U^*(r^2, \omega^*))$. This means $\mathrm{Re}(U)$ is the same for both, indicating confinement, while $\mathrm{Im}(U)$ flips sign and relates to stability: $\mathrm{Im}(U) > 0$ in the confinement region corresponds to $\gamma > 0$ (growing mode, unstable), $\mathrm{Im}(U) < 0$ corresponds to $\gamma < 0$ (decaying mode, stable), and $\mathrm{Im}(U) = 0$ to $\gamma = 0$ (marginally sta-

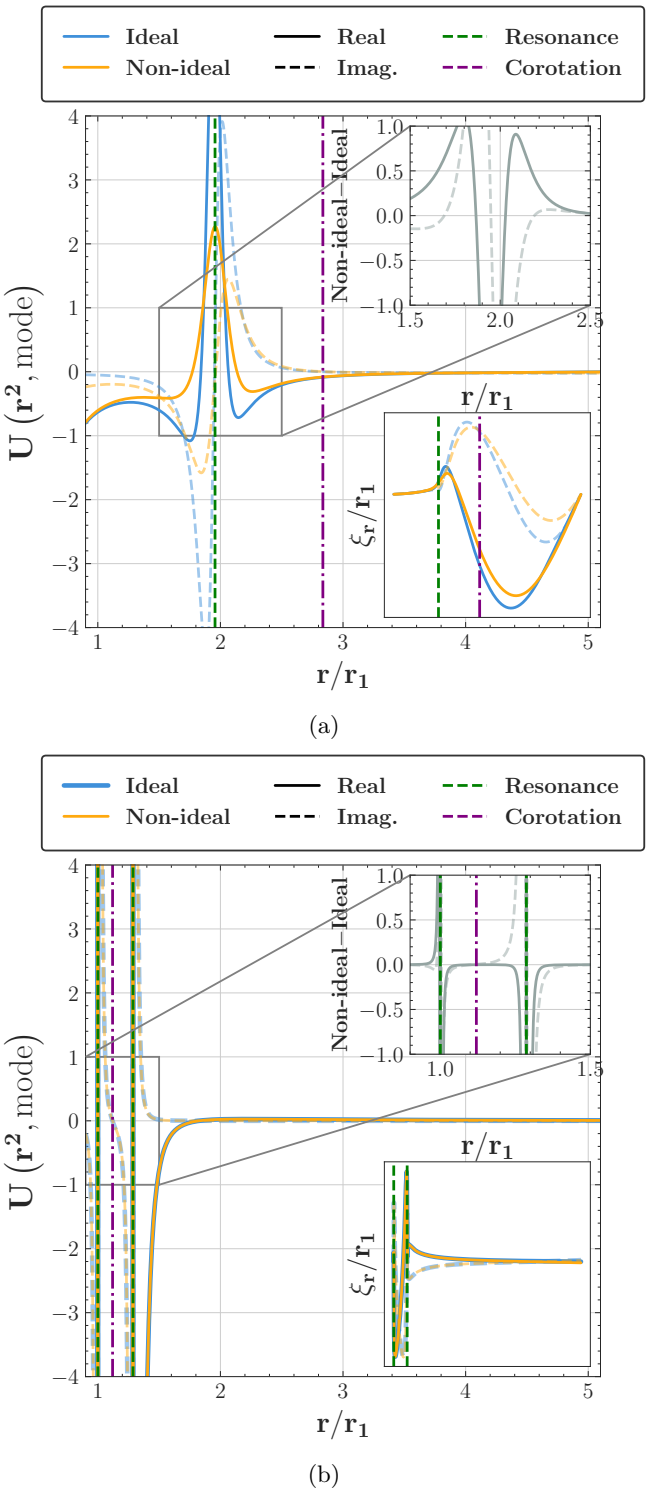

FIG. 6: Potentials for the non-axisymmetric $(m = 1)$ MCI $1k_1$ (a) and MRI $1k_1$ (b) $(r_1 k_1 = \pi/4)$ modes demonstrate diffusive broadening of confinement structure as Rm is increased (Pm = 1, $V_A/(r_1\Omega_0) = 0.2$). Non-ideal shooting for MCI and MRI are conducted at Rm = 105 and Rm = 31623 respectively. In both cases, increased diffusive effects broaden the modes around the resonances, resulting in a more global structure. This broadening is evident in the inset figures, where we plot the difference between the non-ideal and ideal solutions, demonstrating a widening of the ideal profile upon the introduction of diffusion.

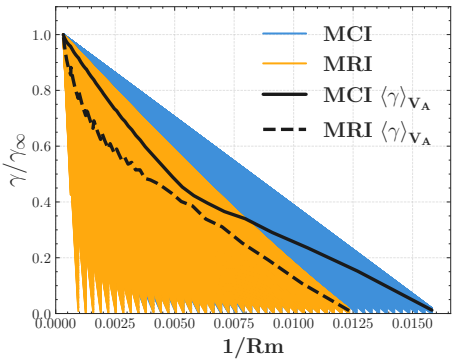

FIG. 7: Growth rate scaling of MRI/MCI modes for a span of $V_A/(r_1\Omega_0)$ shows that MCI modes scale weakly with non-idealities. Finite Rm growth rates γ are normalized to ideal growth rates γ_∞ to consider magnetic-field invariant scaling. Magnetic field average scaling ($\langle\gamma\rangle_{V_A}$) is considered for both MRI and MCI modes. All values are from the non-ideal global shooting method with $k_z = 2k_1$ ($r_1k_1 = \pi/4$) and the AR1 radial aspect ratio. Shooting was conducted with Pm = 1 to consider the largest non-ideal contribution to scaling.

ble). Therefore, in the ideal limit, stability is wholly determined by the sign of γ since it is the only element that contributes to Im(U).

In the non-ideal case, time reversal symmetry of the model is broken. Therefore, stability is no longer determined by the sign of Im(U) (as demonstrated in Figure 8b). Instead, regions where Im(U) is large coincide with Alfvénic resonances acting as dissipative layers. Modes whose amplitude is localized near these regions experience stronger damping (MRI), while more global modes (MCI) that extend across the domain are less sensitive. Thus, the imaginary structure of the potential, Im(U), can still offer insight into mode confinement, but stability must be determined directly via eigenvalue analysis.

We now transform Equation 11 to define the form that a well-defined potential must obey. This approach is similar to [31], except under a different normalization, which makes the quantity we derive an energy. We begin by multiplying Equation 11 by $\Psi^*(r^2)$, and then integrating by parts (noting that Ψ at both boundaries is zero) to arrive at the following definition,

$$E = \frac{\int \left[\left|\Psi'(r^2)\right|^2 + U(r^2)\left|\Psi(r^2)\right|^2 \right] dr^2}{\int \left|\Psi(r^2)\right|^2 dr^2} = 0. \qquad (13)$$

For this integral to be zero, two conditions related to the potential $U(r^2)$ must be met:

1. Real Component: The kinetic energy term $\left|\Psi'\right|^2$ is always positive. Therefore, the potential energy term $U(r^2)\left|\Psi\right|^2$ must contribute a negative real part overall. This implies that Re(U) must be sufficiently negative in the region where the mode exists to allow confinement ($\Psi \neq 0$). A purely positive potential cannot support a confined mode.

2. Imaginary Component: The imaginary part of the integral, $\mathrm{Im}(E) \propto \int \mathrm{Im}(U)\left|\Psi\right|^2 dr^2$ must also be zero. This requires that the imaginary part of the potential, Im(U), must either be identically zero (as in the marginally stable case), or it must change sign within the mode's confinement region such that the positive and negative contributions exactly cancel when weighted by $\left|\Psi\right|^2$. A potential where Im(U) is strictly positive or negative throughout the domain cannot support a confined eigenmode

These criteria provide conditions for physically valid, confined solutions within the effective potential framework.

V. GLOBAL SOLUTIONS UNDER VARIOUS SCANS

This section investigates the behavior and scaling of Magneto-Rotational (MRI) and Magneto-Curvature (MCI) instabilities under variations in non-ideal effects (resistivity η, viscosity ν), flow profiles $\Omega(r)$, and domain geometry. We utilize both linear initial-value simulations with the NIMROD code [27] and the non-ideal global spectral shooting method developed in Section IV. First, we present NIMROD simulations across a range of magnetic Reynolds numbers (Rm) and Lundquist numbers (S) to map dominant instabilities and provide benchmarks (Sec. V A). Subsequently, we introduce *spectral diagrams* constructed using the shooting method to visualize regions of instability and mode dominance (Sec. V A 1). The influence of flow profile variations, including shear, vorticity, and its gradient, on mode structure, onset conditions, and the competition between MRI and MCI is examined (Sec. V B). Finally, the impact of varying domain geometry on mode scaling and dominance is explored using both NIMROD and spectral scans in Section V C.

A. Resistive Scaling - initial value NIMROD vs Non-ideal Shooting

We begin by examining the non-axisymmetric ($m = 1$) stability landscape using linear initial-value NIMROD simulations for both purely azimuthal and purely vertical magnetic field configurations in the AR1 geometry (Fig. 9, Table I), consistent with previous ideal studies [19]. These simulations span across magnetic Reynolds number (Rm $= r_1^2\Omega_0/\eta$) and Lundquist number (S $= r_1V_A/\eta$), holding the Prandtl number fixed at Pm $= \nu/\eta = 1$, representing regimes with the largest cumulative non-ideal contributions. The primary goals are to map the dominant modes across the parameter space,

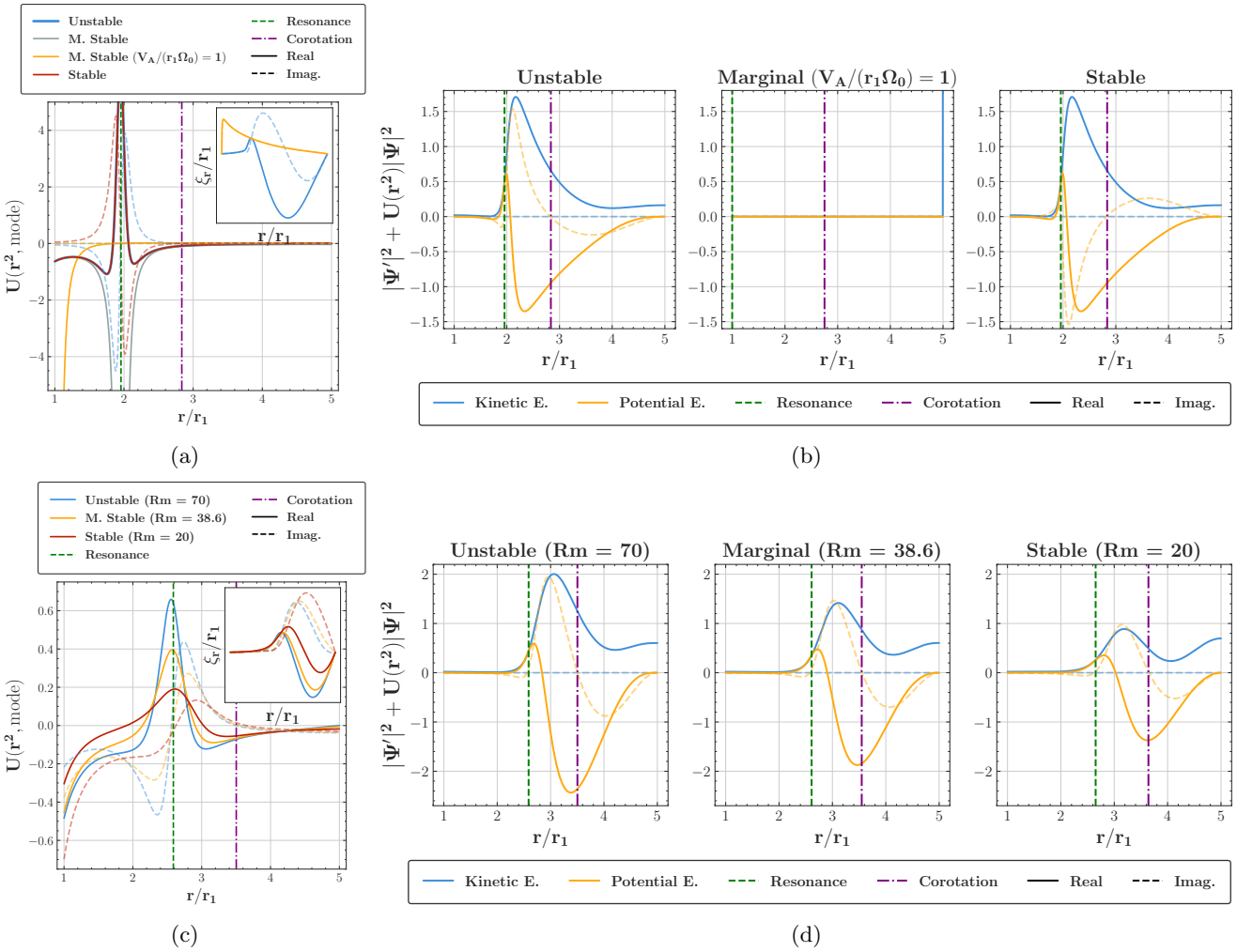

FIG. 8: Stability (sign of γ) of modes confined by ideal ($\mathrm{Rm} = \infty$, no viscosity) potentials (a,b) can be fully determined by the sign of $\mathrm{Im}(U)$, as this is a requirement of the time reversal symmetry inherent in the ideal model. Subfigures (a,b) demonstrate that unstable modes ($\gamma > 0$) have $\mathrm{Im}(U) > 0$, and this similarly follows for stable modes. However, given diffusive effects (c,d), time reversal symmetry is broken and thus stability does not follow solely from the sign of $\mathrm{Im}(U)$, instead indicating dissipative layers around the Alfvénic resonances. All shooting is conducted for the global non-axisymmetric ($m = 1$) MCI $1k_1$ ($r_1 k_1 = \pi/4$) mode at $V_A/(r_1\Omega_0) = 0.2$ (a,b) (stable/unstable) and $V_A/(r_1\Omega_0) = 0.11$ (c,d) unless otherwise stated. All non-ideal potentials consider stability variation as Rm is varied for fixed $\mathrm{Pm} = 1$.

TABLE I: Parameter inputs for global linear NIMROD simulations. Azim. refers to purely azimuthal field and Vert. purely vertical field. All simulations were ran with $r_1 = 0.1\ m$, and $\Omega_0 = 10000 \cdot (10)^{3/2}\ s^{-1}$. For AR0, low magnetic field cases $B_\phi \leq 30$ G were run with a finer temporal resolution $\mathrm{dt} = 10^{-9}$ s compared to $\mathrm{dt} = 10^{-8}$ s of all other Azim. cases. All Vert. cases were run with temporal resolution of $\mathrm{dt} = 10^{-9}$ s. Moreover, $\eta = 2\ m^2/s$ for Vert. was ran with a resolution of 160×160 deg. 4 (m = 1).

radial ratio	aspect	$\mathrm{Rm} = r_1^2\Omega_0/\eta$	$\mathrm{Pm} = \nu/\eta$	$\mathrm{S} = r_1 V_A/\eta$	Config.	Resolution
AR0		6.3E2−3.2E4	1	9.8E0−4.4E2	Azim.	80×80 deg. 4 (m = 1)
AR1		3.2E1−3.2E4	1	4.9E-1−4.4E3	Azim.	80×80 deg. 4 (m = 1)
AR1		3.2E1−3.2E4	1	4.9E-1−4.4E3	Vert.	120×120 deg. 4 (m = 1)
AR2		6.3E2−3.2E4	1	4.9E-1−5.9E3	Azim.	160×160 deg. 4 (m = 1)

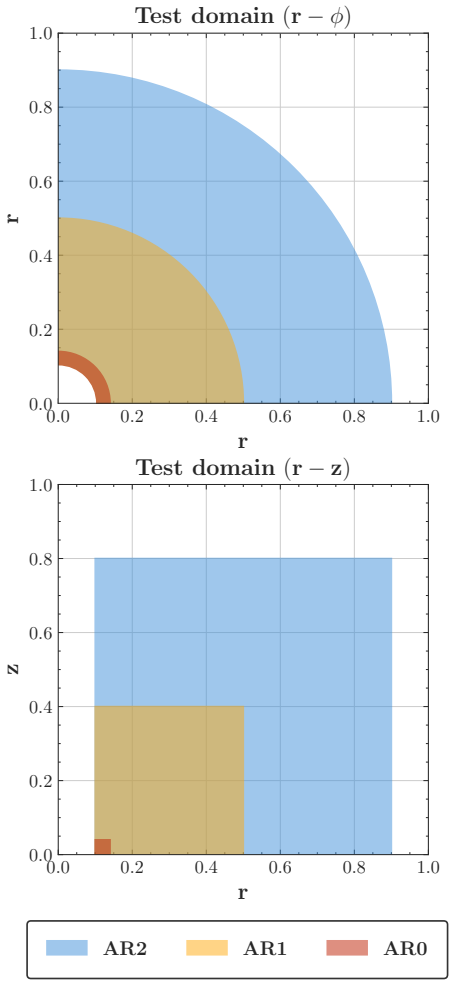

FIG. 9: Discrete slices of system geometry between different disk configurations that were utilized for NIMROD simulation and benchmarking of resistive shooting method. We define all domains such that the vertical aspect ratio is constant $\Delta z/\Delta r = 2$. Meanwhile, AR0, AR1, and AR2 exhibit radial aspect ratios $r_1/\Delta r = r_1/(r_2 - r_1) \in \{5/2, 1/4, 1/8\}$.

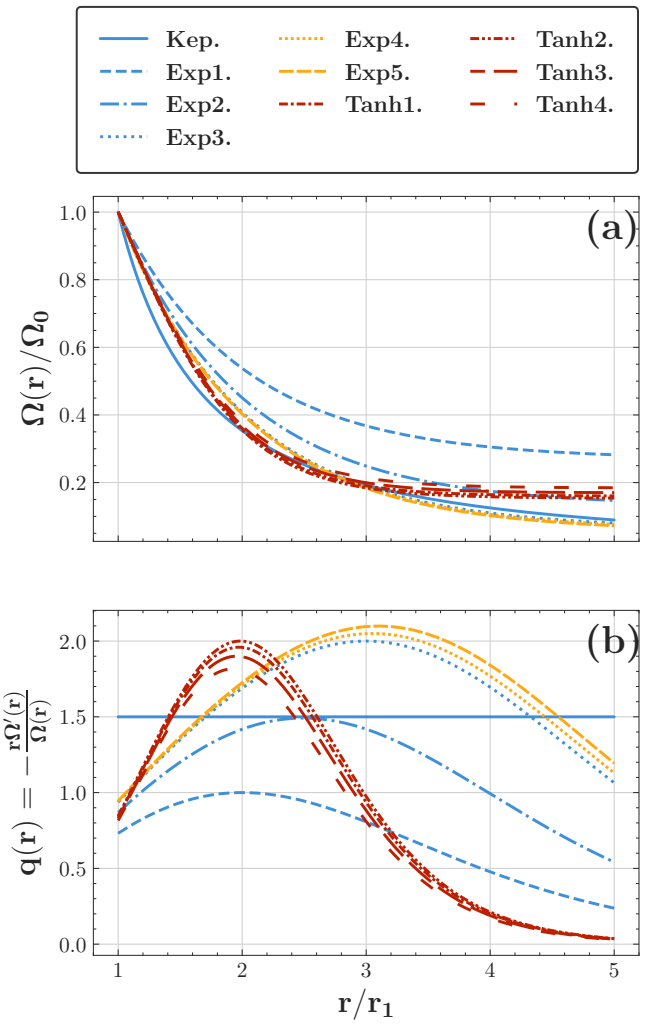

FIG. 10: Variation of flow profile parameters. Depicts both the normalized rotational frequency of the plasma $\Omega(r)/\Omega_0$, as well as the flow shear parameter $q(r) = -\frac{r\Omega'(r)}{\Omega(r)}$. We consider flows unstable to axisymmetric (and thus non-axisymmetric) hydrodynamic perturbations ($1 \leq q(r) \leq 2$). Kep. is the standard Keplerian profile with $\Omega(r)/\Omega_0 = 1/r^{3/2}$. The exponential profiles (Exp.) are generated as $\Omega(r)/\Omega_0 = a\exp(1 - r/r_1) + (1 - a)$. Exp1, Exp2, and Exp3: $a = 0.7312$, $a = 0.8689$, and $a = 0.9366$ respectively. In addition, we consider hydrodynamically unstable configurations ($q(r) > 2$) generated via the exponential profile. Exp4, Exp5: $a = 0.9409$, $a = 0.9448$. All configurations here are shown in the AR1 radial aspect ratio.

identify transitions between MRI and MCI, and generate benchmark data for validating the non-ideal global approximations discussed in Sec. IV A. Ideal spectral solutions derived from Eq. 6 in the limit $\eta, \nu \to 0$ are also computed for various vertical wavenumber (k_z) and serve as a baseline for understanding the mode behavior (shown as curves in Fig. 11). We then extend the spectral solutions to finite Rm/Pm and provide the tools for determining the non-ideal onset of instability.

Two primary types of transitions between dominant modes are observed as Rm and the Lehnert number ($B_0 = V_A/(r_1\Omega_0)$) (proportional to $S/\sqrt{\mathrm{Rm}}$ for fixed r_1, Ω_0) are varied (Fig. 11). First, a transition driven by magnetic field strength can occur if the ideal growth rates of MRI and MCI modes cross. At low V_A, localized MRI modes may dominate, while at higher V_A, global MCI modes become most unstable. This type of transition is evident in the vertical field case (Fig. 11a) but not observed for the ideal modes in the azimuthal field case within the parameter range studied (Fig. 11c). Second, a transition driven by diffusivity occurs due to the different scaling of MRI and MCI growth rates with Rm

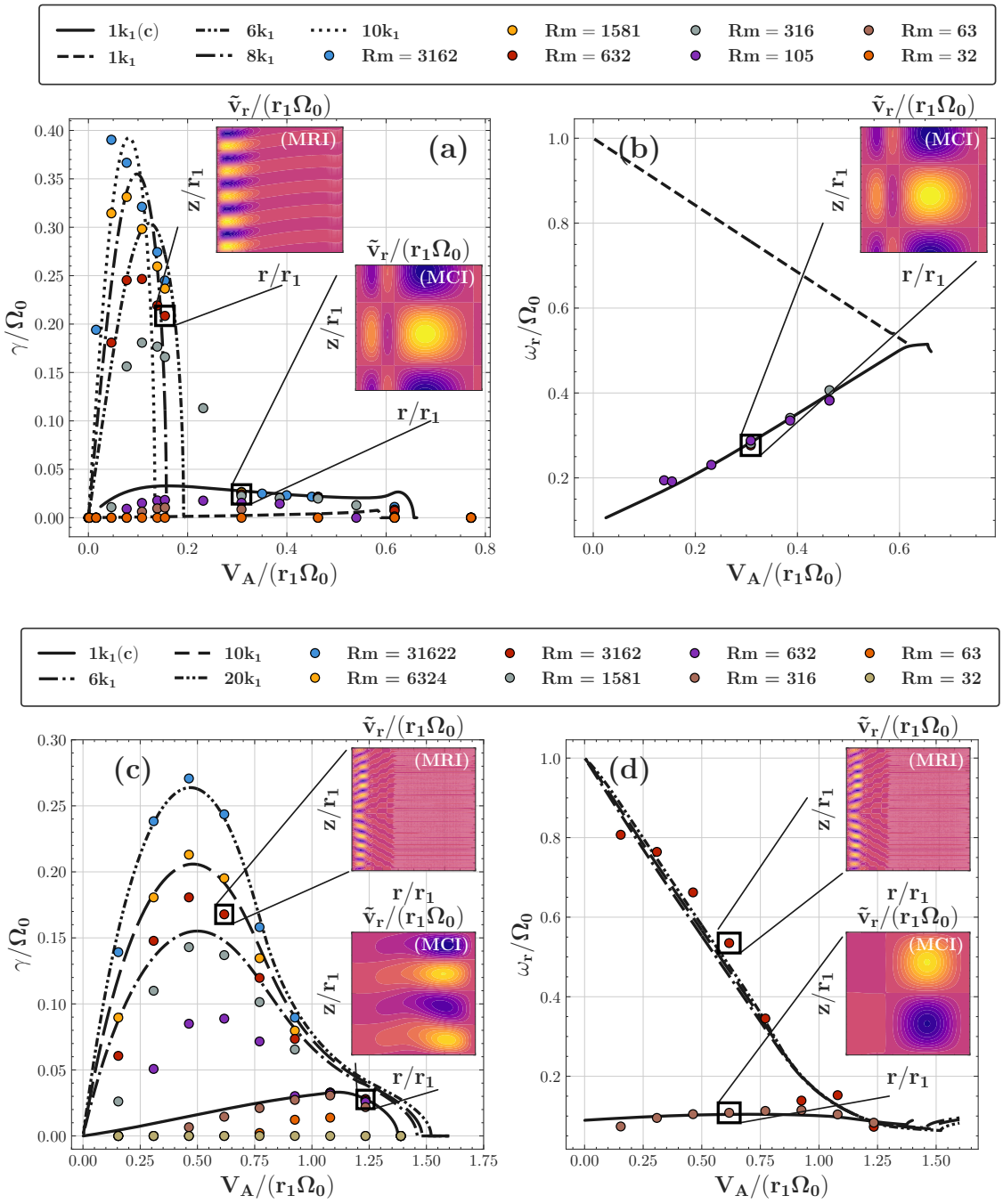

FIG. 11: ($m = 1$) Growth rates and frequencies for pure vertical field (a,b) and azimuthal field (c,d) from both NIMROD simulations (all finite Rm points) and the ideal global shooting method (curves) for relevant vertical wave numbers. In both field configurations, there exists a V_A/V_0 where the system transitions from the localized MRI to global MCI mode. A transition Rm exists where the system becomes the MCI $1k_1$ mode for all V_A/V_0. For a purely vertical field, ideal shooting is conducted for the $1k_1$ MCI mode (denoted as (c)) as well as MRI $1k_1$, $6k_1$, $8k_1$, and $10k_1$ modes. For a purely azimuthal field, ideal shooting is conducted for the $1k_1$ MCI mode (denoted as (c)) and MRI $6k_1$, $10k_1$, and $20k_1$ modes. Inset plots depict observed mode structures from NIMROD simulations showing that the MCI modes are global and low k_z, meanwhile the MRI modes are local and high k_z.

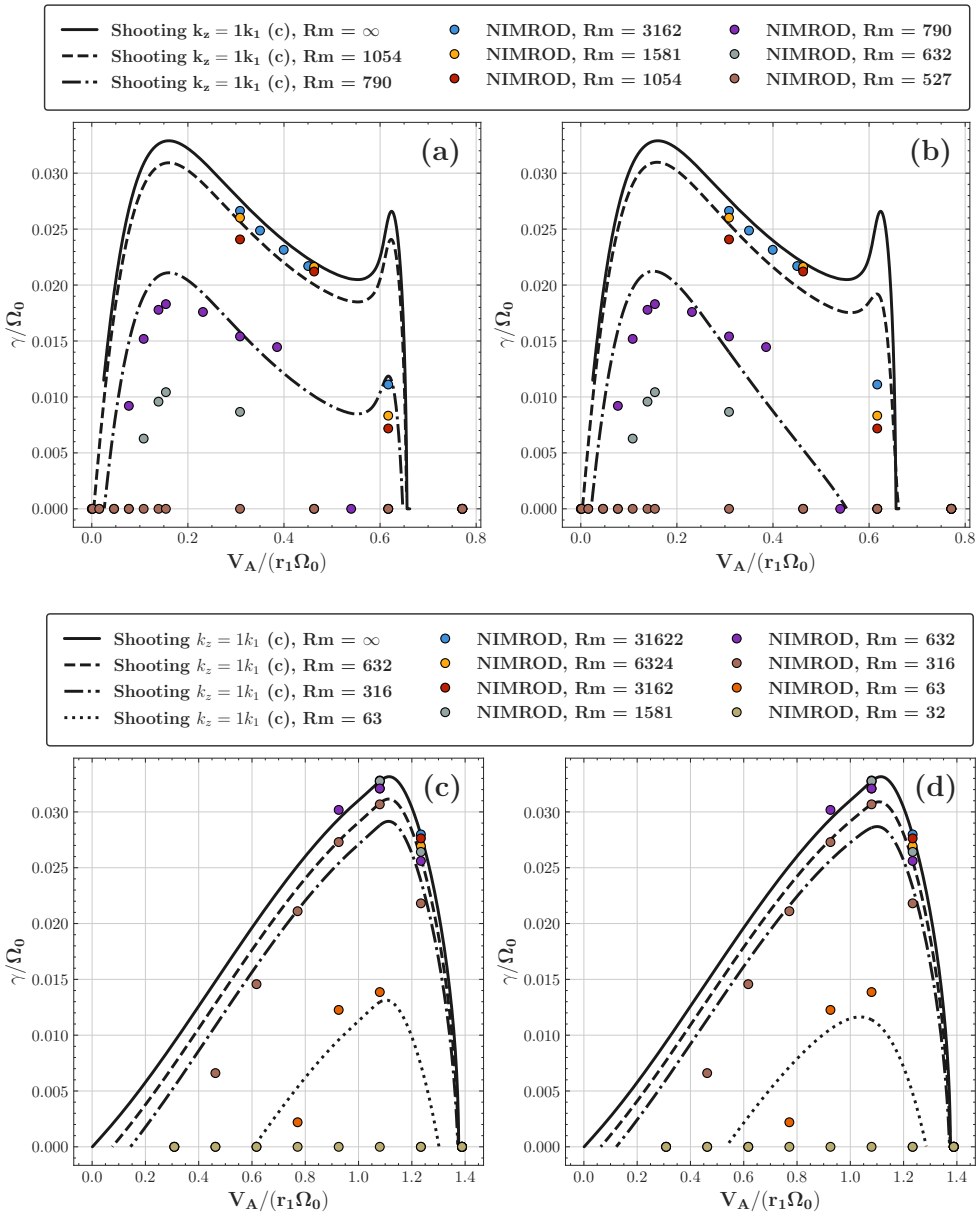

FIG. 12: Benchmarking: ($m = 1$) resistive shooting growth rates vs NIMROD simulations (points) on MCI $1k_1$ ($r_1 k_1 = \pi/4$) mode for both vertical (a,b) and azimuthal magnetic field (c,d). In (a,c) we demonstrate the "TWKB" method and in (b,d) we show the "MWKB" method. All analysis was done with the AR1 radial aspect ratio, and Pm = 1.

(see Sec. IV D). Even if MRI is dominant in the ideal limit or at high Rm, the system is expected to transition to MCI dominance as Rm is decreased, provided MCI is unstable. NIMROD simulations confirm this transition for both field configurations (Figs. 11a,c). These transitions manifest in the simulations as abrupt changes in the mode's frequency and spatial structure, shifting from localized, high-k_z, high-frequency characteristics (MRI) to global, low-k_z, low-frequency features (MCI), as illustrated by the inset mode structures and frequency plots (Figs. 11b,d).

The existence of the location of these transitions depends sensitively on the specific flow profile and domain geometry (explored further in Secs. V B, V C). However, comparing the ideal mode growth rates provides a practical predictive framework. An ideal field-driven transition exists if ideal MRI and MCI growth rates cross. If instead the ideal MRI growth rate envelope (is always larger than) MCI, no field-driven transition occurs. However, a diffusivity-driven transition at low Rm to MCI may exist, provided the MCI is unstable. Conversely, if MCI modes envelope MRI, there will exist no transi-

tions (diffusivity-driven or field-driven) and MCI dominates throughout (see Sec. V C).

We now proceed to demonstrate that the non-ideal global shooting method, incorporating the approximation for diffusive terms, successfully captures these complex dynamics observed in NIMROD. This validation sets the stage for using the computationally efficient shooting method to construct comprehensive *spectral diagrams* for predicting instability boundaries and dominant mode characteristics.

To assess the accuracy of the non-ideal global shooting method and the underlying TWKB and MWKB approximation (Sec. IV A), we compare their predictions against the NIMROD simulation results across varying parameters. Since individual MRI modes ($k_z \geq 1k_1$) often dominate only in narrow regions of parameter space (see Sec. V A 1), the MCI $1k_1$ mode, which typically occupies a larger domain and represents the longest radial wavelength (posing the strongest for the short-wave approximations), is used for detailed benchmarking. Figure 12 compares the growth rates computed using both approximations against NIMROD data for the MCI $1k_1$ mode at Pm = 1.

For the vertical field configuration (Figs. 12a,b), both approximations reproduce the NIMROD growth rates reasonably well at low and intermediate field strengths ($V_A/(r_1\Omega_0)$, where modes tend to be more localized. At high field strengths, where the MCI modes become strongly global, deviations appear: TWKB tends to under-damp (overestimate γ), while MWKB tends to over-damp (underestimate γ) compared to NIMROD. However, since the instability onset occurs at intermediate field strengths, both methods generally capture the onset parameters accurately.

For the azimuthal field configuration (Figs. 12c,d), both approximations show good agreement with NIMROD across the entire range of field strengths tested, even for strongly global modes. Further investigation is needed to determine if this superior performance for an azimuthal field is a general feature.

Given that the MCI mode represents a limit case for the short-wavelength approximations, the reasonable agreement here suggests that the dynamics of the generally more localized MRI modes should also be adequately captured by either method. As discussed in Section IV A, the optimal choice between TWKB and MWKB can depend on the domain configuration. Overall, these results validate the non-ideal global shooting method as a reliable tool for exploring instability characteristics.

1. *Spectral diagrams and the Instability Onset*

A significant advantage of the spectral shooting method is its ability to efficiently compute the entire spectrum of unstable modes (including subdominant ones) for any given set of parameters. This capability allows for the construction of *spectral diagrams*, analogous to phase diagrams, which map the character of the dominant instability across parameter space. Such diagrams provide valuable insights into the stability landscape, mode competition, and instability onset conditions.

Figure 13 presents an example spectral diagram for the vertical field case (AR1 geometry, Keplerian flow, Pm = 1), computed using the MWKB approximation. The diagram plots the dominant mode type (identified by its vertical wavenumber k_z) and its corresponding frequency ω_r as a function of Rm and Lehnert number ($V_A/(r_1\Omega_0)$). The shooting results (colored regions) are overlaid with points indicating the dominant mode identified in corresponding NIMROD simulations. There is excellent agreement between the two methods regarding the region of dominance: high-k_z, high frequency MRI modes prevail at high Rm and low V_A, while the low-k_z, low frequency MCI mode dominates at low Rm and high V_A. The discontinuous jumps in frequency associated with transitions between these regimes are captured. Furthermore, the mode structures computed by the shooting method match those observed in NIMROD (inset plots).

This analysis corroborates the finding from Section IV D that the instability onset (the threshold for any mode to become unstable as Rm or V_A is increased from zero) typically occurs via the global, low-frequency MCI $1k_1$ mode for configurations with sufficient curvature. The spectral diagram method provides a direct visualization of this onset boundary.

These diagrams also have potential implications for the experimental identification of modes. For instance, if Rm can be varied experimentally (e.g., by changing temperature or rotating rate Ω_0), a discontinuous jump in the observed frequency could signify a transition from MCI dominance near onset to MRI dominance at higher Rm, provided the ideal MRI is unstable under those conditions.

Similarly, in Figure 14 we demonstrate that these methods (both resistive shooting and spectral diagrams) extend to general Prandtl Number and azimuthal mode number. Though as we demonstrate, classifications of instability near onset likely only requires scans of the $m = 0$ and $m = 1$ modes.

The spectral diagram approach is a versatile tool. We employ it further in Section V B to investigate how flow profiles modify instability domains, mode characteristics, and onset criteria, demonstrating its utility for systematic parameter exploration relevant to astrophysical and laboratory plasmas. Importantly, in this section we demonstrate the non-axisymmetric onset of instability still occurs at a global MCI mode with a profile (and viscosity) similar to that utilized and observed in experiments (see Section V B, Figure 21, [10, 20, 33]).

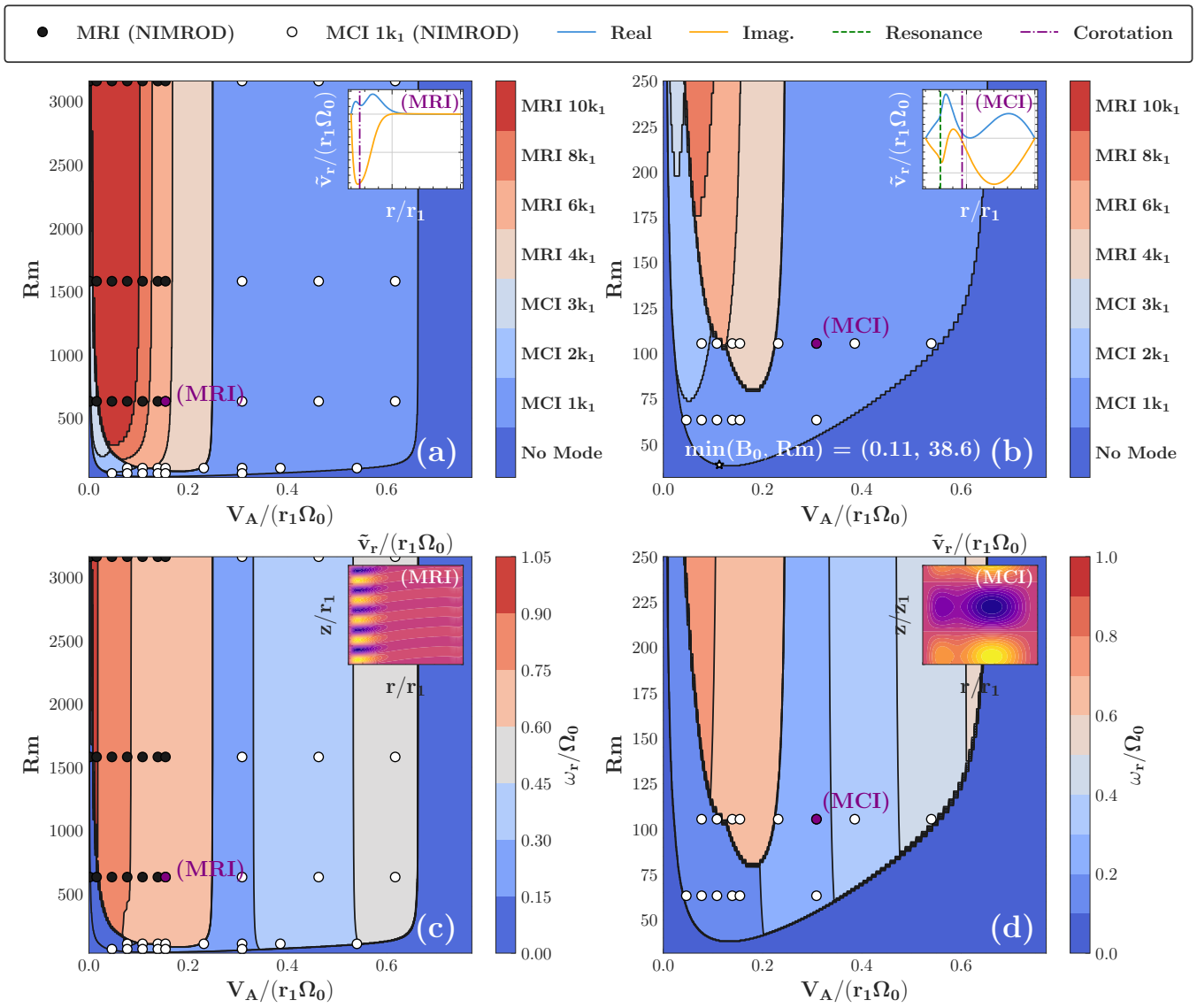

FIG. 13: Vertical field dominant mode scans over Rm and $V_A/(r_1\Omega_0)$ from non-ideal shooting code and NIMROD (black and white numerical points) for Pm = 1 and the Keplerian profile. (a) shows growth rate results for high Rm, and (b) shows low Rm (color bar shows various k_z). At high Rm and low fields, high k_z MRI modes dominate, whereas at low Rm and high fields, low k_z MCI modes dominate. (c) illustrates frequencies (ω_r) at given Rm and V_A for the dominant mode, and (d) shows the same relationship for low Rm. All eigenvalue analysis was done via the resistive global shooting method for non-axisymmetric ($m = 1$) modes with $r_1k_1 = \pi/4$, $k_r^2(r) = \pi^2/r^2$ (MWKB), and $r_2 - r_1 = 4r_1$ (AR1). We show even k_z for MRI up to $k_z = 10k_1$ for simplicity; however, more modes do coexist and are seen via NIMROD simulations. Inset plots show mode structure from the non-ideal global shooting method (a,b), and NIMROD simulations (c,d).

B. Flow Configuration

While Keplerian flow ($\Omega(r) \propto 1/r^{3/2}$) is a standard benchmark motivated by astrophysical context and its stability to axisymmetric hydrodynamic perturbations (per the Rayleigh criterion), realistic flows can deviate significantly. This section investigates how variations in the background flow profile $\Omega(r)$, specifically altering the vorticity $\Gamma = (\nabla \times \mathbf{v}_0)_z = (1/r)d(r^2\Omega)/dr$ and its radial gradient ($\Gamma' = 3\Omega' + r\Omega''$), influence the stability, structure, and competition of non-axisymmetric ($m = 1$) MHD modes, particularly MRI and MCI.

We choose to decouple flow characteristics with vorticity specifically because it demonstrates the competition between shear and curvature. By definition, we can describe the components of Γ as,

$$\Gamma(r) = \frac{1}{r}\frac{d}{dr}\left(r^2\Omega(r)\right) = 2\Omega + r\Omega' = \Omega\left(2 - q(r)\right) \quad (14)$$

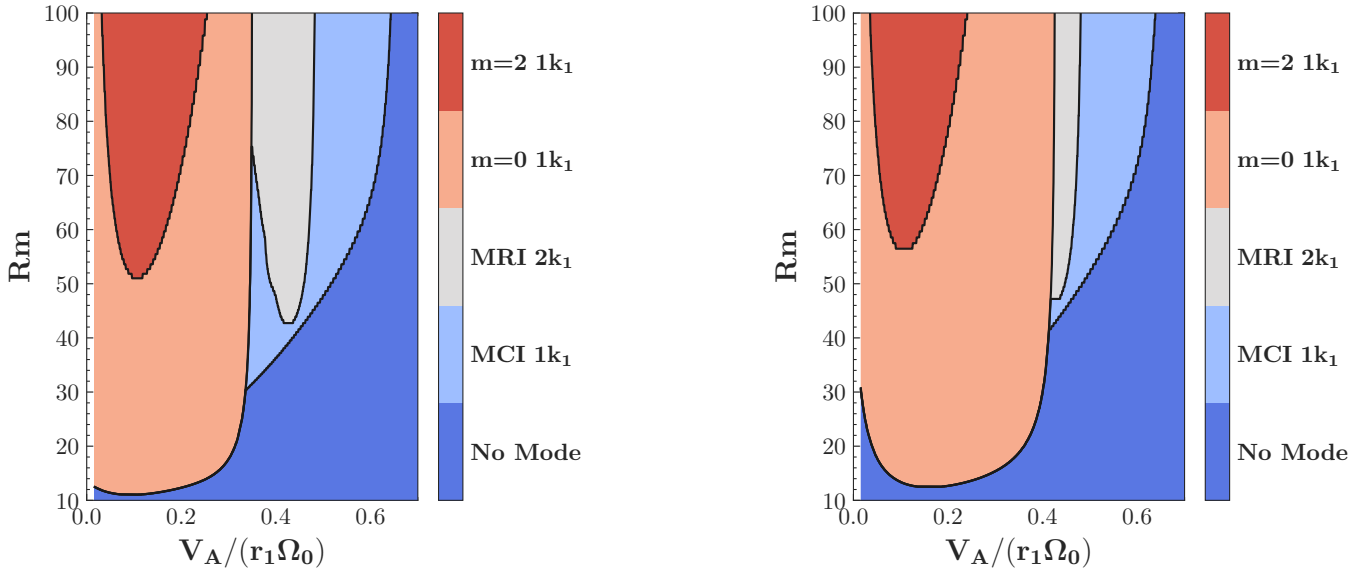

(a) $\mathrm{Pm} = 10^{-6}$ (b) $\mathrm{Pm} = 10^{-1}$

FIG. 14: Vertical field dominant modes at low Rm from the non-ideal global shooting method at low fluid viscosity ($\mathrm{Pm} = 10^{-6}, (a)$) and intermediate fluid viscosity ($\mathrm{Pm} = 10^{-1}$, (b)). Here, we show the dominant modes for $m = 0$, $m = 1$ (MRI and MCI), and $m = 2$ (as denoted in the color bar). All analysis was conducted for $r_1 k_1 = \pi/4$, $k_r^2(r) = \mathrm{MWKB}$, $r_2 - r_1 = 4r_1$ (AR1), and the Keplerian flow configuration. We find that at low Rm and low fields, the most global axisymmetric mode is the dominant instability, whereas at high fields the global MCI $1k_1$ mode becomes dominant for both low and intermediate viscosities.

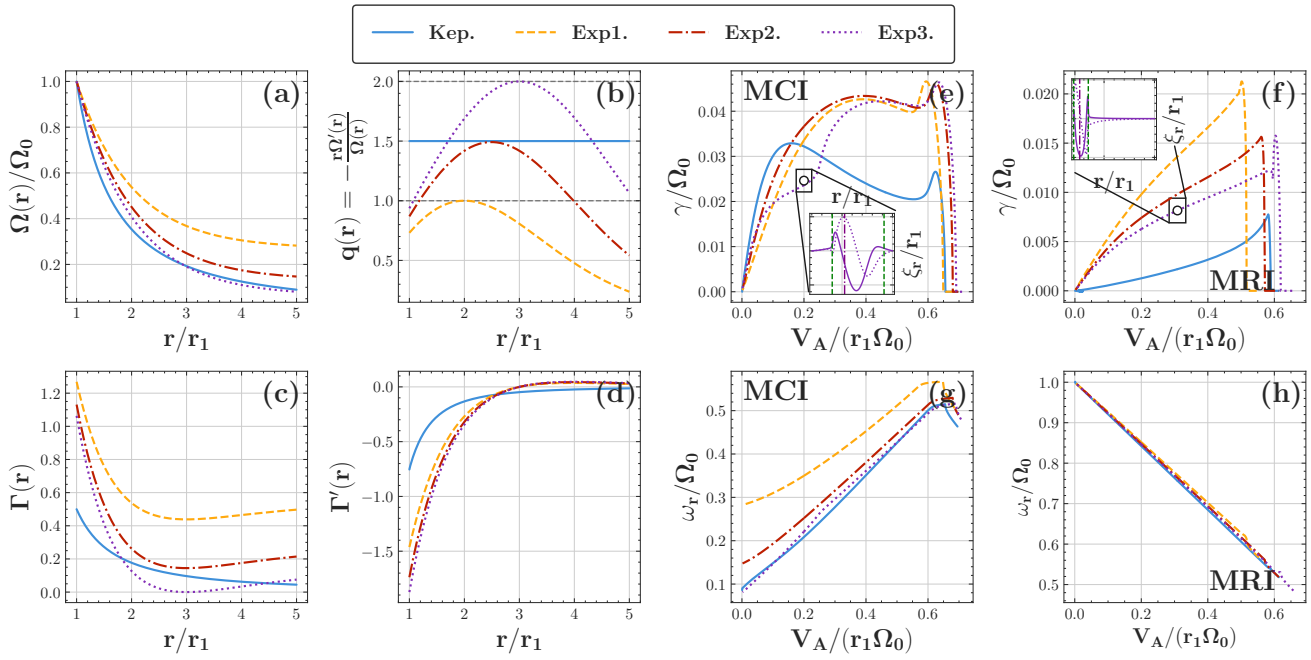

FIG. 15: Flow configuration (a,b,c,d), growth rates (e,f), and frequencies (g,h) for the Keplerian and Exponential flow configuration. We define the Exponential profile as $\Omega(r)/\Omega_0 = a\exp(1 - r/r_1) + (1 - a)$. Exp1: $a = 0.7312$; Exp2: $a = 0.8689$; Exp3: $a = 0.9366$. All shooting (e,f,g,h) was conducted for the non-axisymmetric ($m = 1$), $k_z = 1k_1$ ($r_1 k_1 = \pi/4$) modes with a purely vertical magnetic field. We define Exp1 such that $\mathrm{Max}(q(r)) = 1$, Exp2 such that $\mathrm{Max}(q(r) = 3/2$, and Exp3 such that $\mathrm{Max}(q(r) = 2$. The exponential profile can be tuned for $\mathrm{Max}(q(r)$ $= 5$ ($a = 1$). However, we chose a maxima of $q(r) = 2$ to include only MHD perturbations. While the MRI modes are uniformly damped by increased relative flow curvature, the MCI modes persist at large vorticities.

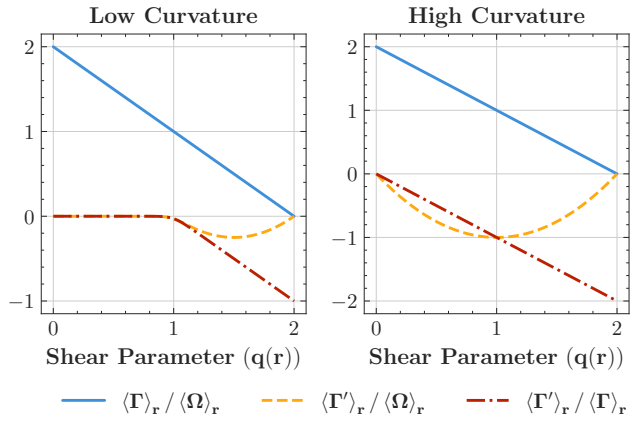

FIG. 16: Scaling of relative vorticity ($\langle\Gamma\rangle_r / \langle\Omega\rangle_r$), relative vorticity gradient ($\langle\Gamma'\rangle_r / \langle\Omega\rangle_r$), and relative flow curvature ($\langle\Gamma'\rangle_r / \langle\Gamma\rangle_r$) demonstrate significant dependence of relative contributions on the curvature of the domain. Low Curvature corresponds to $r_2/r_1 \to \infty$, whereas High Curvature corresponds to $r_2/r_1 \to 1$. Scaling emphasizes that vorticity gradients become an increasingly important contribution in highly curved domains.

for $q(r)$ the standard shear parameter. Specifically, the first component describes rigid body rotation due to curvature of the flow, whereas the latter describes shear. Vorticity's gradient ($\Gamma' = 3\Omega + r\Omega'' = -(\frac{q(2-q)}{r\Omega} + \Omega q')$) thus describes how rapidly the competition between curvature and shear varies along the disk.

We utilize this framework to explore regimes both stable and unstable to hydrodynamic (HD) perturbations, including non-axisymmetric instabilities that can arise when the flow is Rayleigh-stable ($q(r) = -\frac{r\Omega'}{\Omega} < 2$). We demonstrate that MHD onset conditions are sensitive to the flow profile, although the global MCI $1k_1$ mode typically remains the first to become unstable. Furthermore, we analyze the bifurcation of the MCI mode into a hydrodynamic branch in HD-unstable flows and develop a criterion to predict the MHD onset threshold based upon resonance dynamics.

1. *Vorticity and the Flow Curvature Effect*

We now investigate the influence of vorticity, $\Gamma(r)$, and its radial gradient Γ' on MHD stability. By introducing three additional profiles with tunable shear (and thus vorticity) (Exp1-3, see Fig. 15), we reveal that both MRI and MCI modes are significantly more unstable under these flows than the Keplerian profile, even in configurations with $q(r)$ close to the Keplerian profile (cf. Kep and Exp3). To understand the underlying mechanisms, we recast the effective potential formalism (see Sec. IV D) for a purely vertical field, explicitly separating terms involving Γ, Γ' to demonstrate their individual destabilizing effects:

$$U(r^2, \text{mode}) = f_1 + \Gamma f_2 + \Gamma^2 f_3 + \Gamma' f_4 \tag{15}$$

with,

$$f_1 = \frac{k_z^2 r^2 + m^2 - 1}{4r^4} + \frac{k_z^2}{4r^2}\left(\frac{k_z^2 r^2 - 2m^2}{k_z^2 r^2 + m^2}\right) - \frac{\Omega^2\left(k_z^2 + m^2\right)\omega_A^2}{r^4\left(\omega_A^2 - \bar{\omega}^2\right)^2} + \frac{m\Omega\bar{\omega}}{r^4\left(\omega_A^2 - \bar{\omega}^2\right)}\left(\frac{2k_z^2 r^2 + m^2}{k_z^2 r^2 + m^2}\right)$$
$$- \frac{\Omega\bar{\omega}}{r^4}\left(\frac{k_z^2 r^2\left(m^2+1\right) + m^4}{k_z^2 r^2 + m^2}\right), \quad f_2 = \frac{m^2\bar{\omega}^2\Omega}{r^4\left(\omega_A^2 - \bar{\omega}^2\right)^2} + \frac{\Omega\left(k_z^2 r^2 + 2m^2\right)}{2r^4\left(\omega_A^2 - \bar{\omega}^2\right)} - \frac{m\bar{\omega}k_z^2}{2r^2\left(k_z^2 r^2 + m^2\right)\left(\omega_A^2 - \bar{\omega}^2\right)}, \tag{16}$$
$$f_3 = -\frac{m^2\omega_A^2}{4r^4\left(\omega_A^2 - \bar{\omega}^2\right)^2}, \text{ and } f_4 = \frac{m\bar{\omega}}{4r^3\left(\omega_A^2 - \bar{\omega}^2\right)}$$

The coefficients f_1, f_2, f_3, f_4 depend on the system parameters and the mode's growth rate/frequency (γ, ω_r). The term f_1 contains contributions independent of vorticity and its gradient, including curvature and flow energy. Meanwhile, f_2, f_3 capture the linear and quadratic vorticity effects, whereas f_4 captures the effect of Γ'.

Figure 17 illustrates the decomposition (Eq. 16) for representative MCI and MRI modes using Keplerian and exponential flows (Exp1-Exp3, defined in Fig. 15). While the non-vorticity term f_1 generally provides the largest contribution to the potential well/barrier structure, the terms involving Γ ($\Gamma f_2 + \Gamma^2 f_3$) and Γ' ($\Gamma' f_4$) can significantly modify the potential, influencing mode localization and stability. The sign and magnitude of these contributions depend intricately on the mode type (via ω, $\bar{\omega}$), field strength (via ω_A), and flow properties (Ω, Γ, Γ').

To gain qualitative insight, we consider the expected signs of $\bar{\omega}$ and $(\omega_A^2 - \bar{\omega}^2)$ in different regimes (Table II). For typical low-frequency MCI modes ($\bar{\omega} < 0$) at low field strength ($\omega_A^2 < \bar{\omega}^2$), both f_2, f_3 terms (related to Γ) and the f_4 term (related to Γ') tend to b e positive (assuming $\Gamma > 0$, $\Gamma' < 0$ as in typical disk profiles), contributing to potential barriers (stabilizing). Conversely, for typical high-frequency MRI modes ($\bar{\omega} > 0$) at low field, these

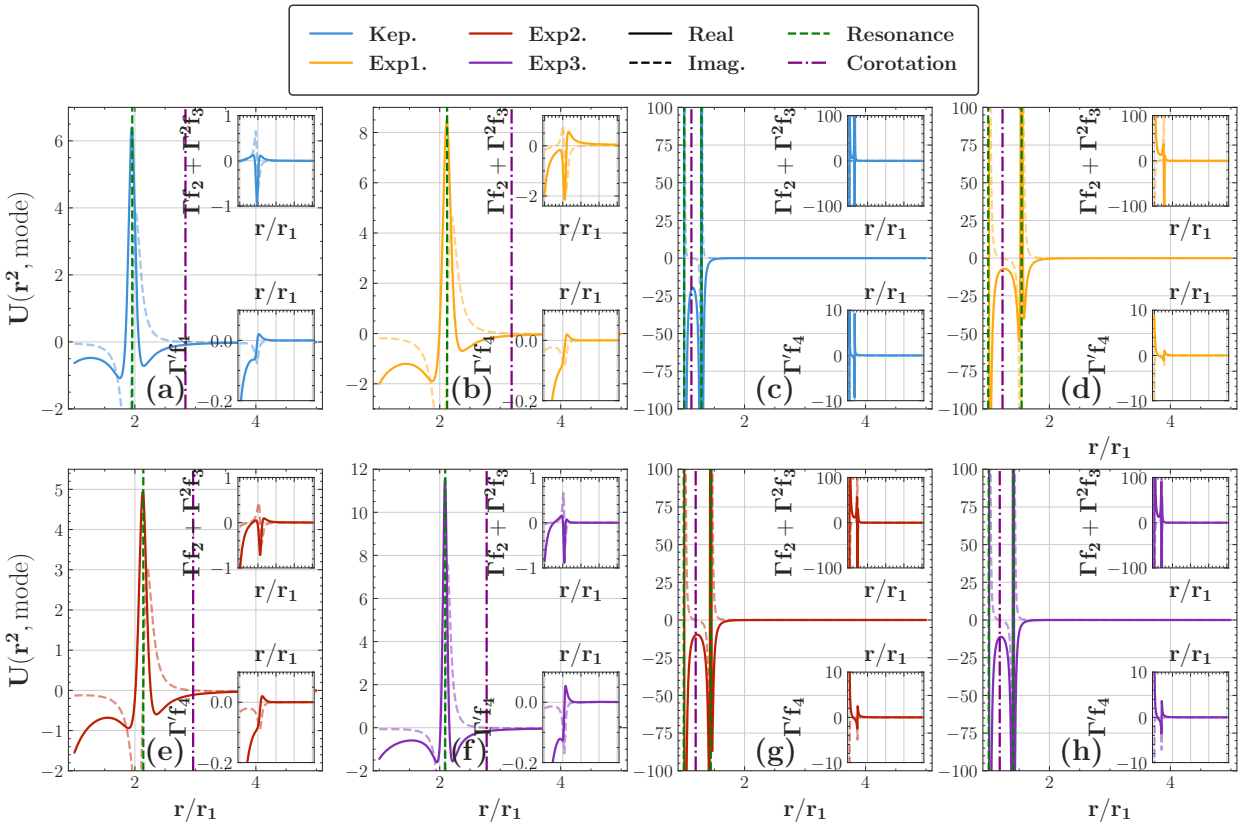

FIG. 17: Vertical field potentials for MCI $1k_1$ (a,b,e,f) and MRI $1k_1$ (c,d,g,h) modes at $V_A/(r_1\Omega_0) = 0.2$ for four flow configurations (Kep (a,c), Exp1 (b,d), Exp2 (e,g), and Exp3 (f,h)). Upper right inset figures show vorticity (Γ) contribution to potential, and lower right inset figures show vorticity gradient (Γ') contribution.

terms tend to be negative, deepening the potential well (destabilizing). The denominators change sign at intermediate fields where $\bar{\omega}^2 \approx \omega_A^2$, reversing some trends. At high fields ($\omega_A^2 > \bar{\omega}^2$), the low-field characteristics are reversed for MRI and MCI, respectively, as mode frequency uniformly decreases/increases for MRI/MCI. Therefore, at high fields ($\omega_A^2 > \bar{\omega}^2$), MCI modes ($\bar{\omega} > 0$) tend to be stabilized by Γ, but destabilized by Γ'. Conversely, MRI modes at high fields ($\bar{\omega} < 0$) tend to be destabilized by Γ and stabilized by Γ'. These heuristics align with the low-field examples in Figure 17.

Further insight comes from estimating vorticity and vorticity gradient scaling characteristics by expanding arbitrary flow configurations as power law profiles: $\Omega(r)/\Omega_0 = 1/r^q$. Vorticity and its gradient can then be expanded as,

$$\Gamma = \frac{(2-q)\,\Omega_0}{r^q},\ \Gamma' = -q\frac{(2-q)\,\Omega_0}{r^{q+1}} \tag{17}$$

Given that Γ, Γ', and Ω are intrinsically coupled, we will define three quantities to classify independent scaling. We first define relative vorticity $\langle\Gamma\rangle_r / \langle\Omega\rangle_r$, which quantifies how the average local fluid rotation (vorticity) scales relative to the average global circulation (Ω). In effect, this distinction separates flows dominated by their intrinsic spin from those dominated by orbital motion. Similarly, the relative vorticity gradient $\langle\Gamma'\rangle_r / \langle\Omega\rangle_r$ defines how rapidly the rotational structure–the balance of curvature and shear–of the fluid changes with radius, with respect to the overall rotation of the system. This parameter is particularly critical when considering shear layers (indicated by a large value) or a laminar flow (small

TABLE II: Scaling of field-dependent MCI and MRI terms to show scaling of vorticity (gradient) terms with different field strengths. (C) and (R) refers to MCI and MRI modes, respectively. Meanwhile, (1) and (-1) refer to destabilizing and confining, respectively. Finally, we consider three field strengths: Low, Intermediate (Interm.), and High.

Field Strength	$\langle\bar{\omega}\rangle_r$	$\langle\omega_A^2 - \bar{\omega}^2\rangle_r$	$\langle\Gamma f_2 + \Gamma^2 f_3\rangle_r$	$\langle\Gamma' f_4\rangle_r$
Low (C/R)	-1/1	-1	-1/1	-1/1
Interm. (C/R)	-1/1	1/-1	1	1
High (C/R)	1/-1	1	1/-1	-1/1

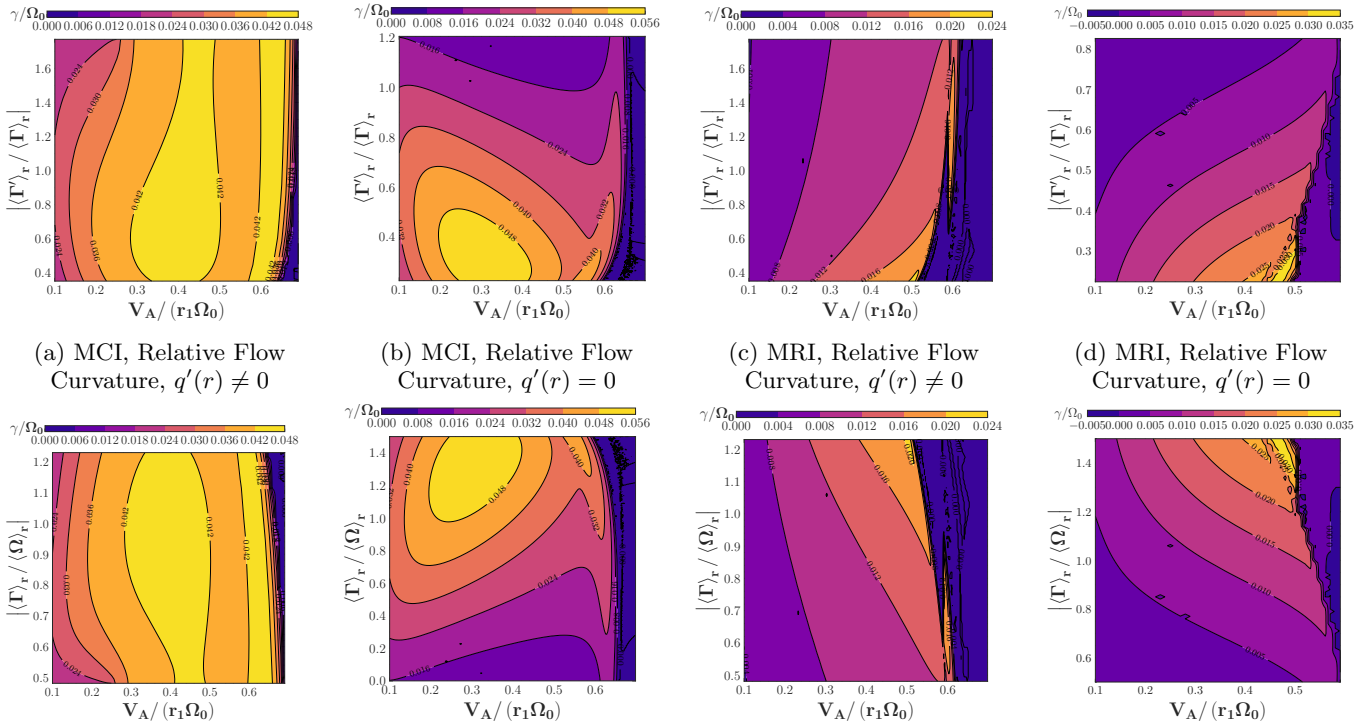

(a) MCI, Relative Flow Curvature, $q'(r) \neq 0$

(b) MCI, Relative Flow Curvature, $q'(r) = 0$

(c) MRI, Relative Flow Curvature, $q'(r) \neq 0$

(d) MRI, Relative Flow Curvature, $q'(r) = 0$

(e) MCI, Relative Vorticity, $q'(r) \neq 0$

(f) MCI, Relative Vorticity, $q'(r) = 0$

(g) MRI, Relative Vorticity, $q'(r) \neq 0$

(h) MRI, Relative Vorticity, $q'(r) = 0$

FIG. 18: Growth rate scan of most unstable non-axisymmetric (MCI (a), MRI (b)) modes for $k_z = 1k_1$ as relative flow curvature ($\langle\Gamma'\rangle_r / \langle\Gamma\rangle_r$) and magnetic field strength are varied for a purely vertical field. In (a,c,e,g), we utilize the Exp. profile ($\Omega(r)/\Omega_0 = a\exp(1 - r/r_1) + (1 - a)$) with non-uniform $q(r)$ ($q'(r) \neq 0$), and vary $\langle\Gamma'\rangle_r / \langle\Gamma\rangle_r$ and $\langle\Gamma\rangle_r / \langle\Omega\rangle_r$ by changing a. We span from the Exp1 to the Exp3 profile to only study the dynamics of MHD perturbations. Similarly, in (b,d,f,h), we consider profiles with uniform $q(r)$ ($\Omega(r)/\Omega_0 = 1/r^q$, spanning between $q = 1/2$ to $q = 3/2$ (Keplerian). MCI modes remain dominant for both small vorticity and large vorticity gradients, with the domain of instability narrowing at large relative flow curvatures. Conversely, the MRI modes are destabilized by vorticity gradients and remain unstable only for low relative flow curvatures.

values). Finally, the relative flow curvature $\langle\Gamma'\rangle_r / \langle\Gamma\rangle_r$ provides a normalized measure of the global competition between shear and curvature across the flow. Importantly, this provides a measure of whether a flow is shear-dominated (large value) or curvature-dominated (low value). For constant q, we can explicitly construct these relations as,

$$\frac{\langle\Gamma\rangle_r}{\langle\Omega\rangle_r} = 2 - q, \quad \frac{\langle\Gamma'\rangle_r}{\langle\Omega\rangle_r} = (2 - q)(1 - q)\frac{r_2^{-q} - r_1^{-q}}{r_2^{1-q} - r_1^{1-q}}, \quad \frac{\langle\Gamma'\rangle_r}{\langle\Gamma\rangle_r} = (1 - q)\frac{r_2^{-q} - r_1^{-q}}{r_2^{1-q} - r_1^{1-q}} \tag{18}$$

The relative vorticity indicates that configurations with lower shear (smaller q) will have higher vorticity contributions to confinement of the mode. Importantly, the scaling with vorticity is a domain-independent quantity. Conversely, the relative vorticity gradient and relative flow curvature are intrinsically domain-dependent quantities, as they are inherently curvature-dependent terms. This is because the definition of vorticity gradient inherently considers the curvature of the flow configuration ($\Gamma' \propto \nabla_r^2\Omega$ in cylindrical coordinates). We can tabulate these scaling relations taking into account domain configuration (see Fig. 16). We find that the contribution of vorticity gradients and relative flow curvature is maximized in domains with large curvature ($r_2/r_1 \to 1$), and minimized in domains with low curvature ($r_2/r_1 \to \infty$). This suggests that the destabilizing effect of Γ' on intermediate-field MCI might be enhanced in strongly curved geometries, potentially contributing to MCI dominance in such domains (cf. Sec. V C). We include the relative vorticity gradient and relative flow curvature to decouple Γ, Γ' scaling when varying parameters underlying the flow configuration.

To verify these scalings numerically, we performed ideal spectral scans using the shooting method, varying the flow profile using both exponential profiles (non-uniform q) and power-law profiles (uniform q) (see Fig. 18). The results broadly confirm the theoretical expectations. We confirm that MCI/MRI growth rates gen-

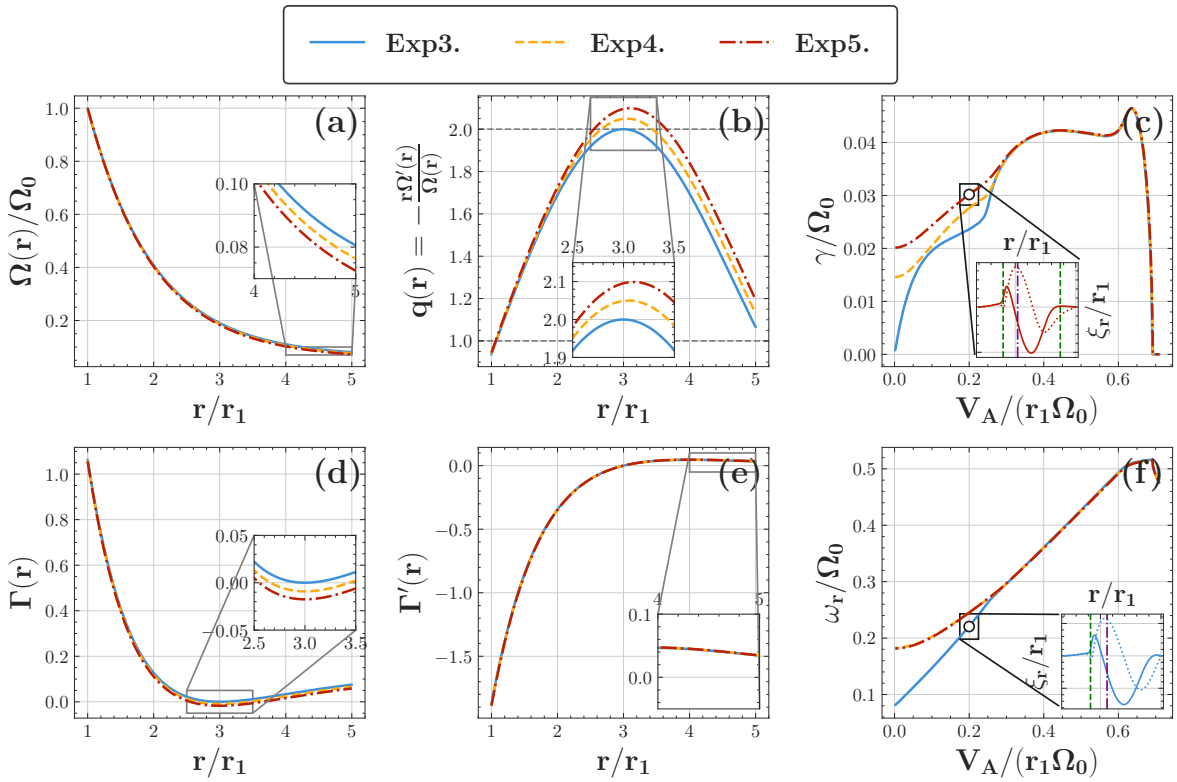

FIG. 19: Flow rate configuration (a,b,d,e), growth rates (c), and frequencies (f) for the Exponential flow configuration demonstrate bifurcation of the MCI mode into hydrodynamic branch as $q(r)$ crosses two. We define the Exponential profile as $\Omega(r)/\Omega_0 = a\exp(1 - r/r_1) + (1 - a)$. Exp3: $a = 0.9366$; Exp4: $a = 0.9409$; Exp5: $a = 0.9448$. All shooting (c,f) was conducted for the non-axisymmetric ($m = 1$), $k_z = 1k_1$ ($r_1k_1 = \pi/4$) modes with a purely vertical magnetic field.

erally increase with higher relative vorticity, and are suppressed by relative flow curvature. Typically, MRI modes scale relatively uniformly with variation of parameters, whether the underlying flow has uniform or non-uniform $q(r)$ (cf. Figs 18c,g and Figs. 18d,h). However, MCI is much more sensitive to the uniformity of the profile (cf. Figs 18a,e and Figs. 18b,f). Since the non-uniformity in the profile $q(r)$ can be equivalently described as flow curvature, this reinforces the concept that MCI is a curvature-driven instability. In contrast, MRI is relatively agnostic due to its local nature. We thus argue that profiles with non-uniform q will generally be more unstable, as onset will still occur at the MCI mode (see Sec. V B 3). These findings emphasize the sensitivity of MHD stability to the detailed flow structure. Investigating more complex profiles, such as those that exhibit local minima in the vorticity (as observed in recent simulations [20]), is a promising direction of future work.

2. *Hydrodynamic Modes*

When the background flow is unstable to hydrodynamic (HD) perturbations, MHD modes can interact and merge with HD modes. The MCI branch, in particular, smoothly connects to an HD instability branch as the magnetic field strength approaches zero ($V_A \to 0$) if the flow permits HD instability. Though we typically consider HD stable flows, we will demonstrate that these hybrid HD-MCI modes exhibit a resonance-localized mode structure, and given a vorticity well, can occur at shear parameters below the Rayleigh criterion.

We begin by studying the traditional Rayleigh criterion through the vorticity framework ($\Gamma = \Omega(2 - q(r))$), as it provides a physically motivated mechanism for defining the onset of hydrodynamic instability. By construction, Γ changes sign at any point where $q(r)$ crosses two (Rayleigh criterion). At these points, Γ' physically acts as a restoring force, thus confining hydrodynamic perturbations (see Fig. 19). This same argument then implies that power-law profiles cannot exhibit hydrodynamic instability, even for $q > 2$, as q is constant, and thus no vorticity well can be formed. We will also demonstrate that this argument implies that profiles with sufficiently deep vorticity wells can exhibit hydrodynamic instability for $q < 2$.

To demonstrate the hydrodynamic onset mechanism, we therefore must consider profiles with non-uniform $q(r)$, such as those generated via the tanh or exponential functions, or those considered by [23]. In Figure 19 we

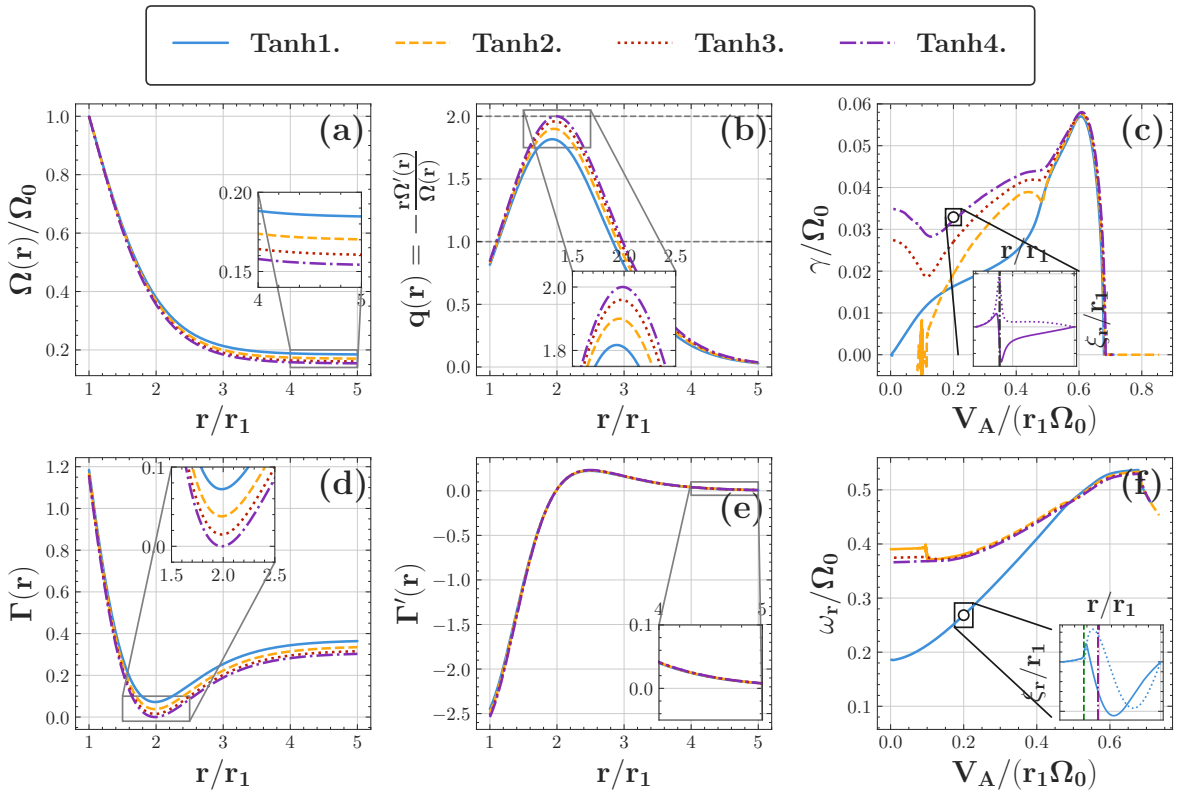

FIG. 20: Flow rate configuration (a,b,d,e), growth rates (c), and frequencies (f) for the Tanh flow configuration demonstrate that vorticity wells can create a hydrodynamic branch for $q < 2$. We define the Tanh profile as $\Omega(r)/\Omega_0 = a\exp(1 - r/r_1) + 1$. Tanh1: $a = 0.8158$; Tanh2: $a = 0.8303$; Tanh3: $a = 0.8400$; Tanh4: $a = 0.8463$. All shooting (c,f) was conducted for the non-axisymmetric ($m = 1$), $k_z = 1k_1$ ($r_1k_1 = \pi/4$) modes with a purely vertical magnetic field.

perturb a HD stable flow configuration (Exp3) to form two HD unstable profiles (Exp4 and Exp5) by varying q. We find that marginally stable profiles (e.g., Exp3) will exhibit knees in the profile that bifurcate upon perturbation of q. We observe this behavior in the Exp4 and Exp5 profiles, which become increasingly hydrodynamically unstable (i.e. have finite growth rates at zero magnetic field, B_0) as $q(r)$ increases. It was also recently observed that profiles with vorticity wells can exhibit hydrodynamic instability for $q(r) < 2$ as shown by [23] and illustrated here using the Tanh profiles (see Fig. 20). Physically, Γ' acts to confine the modes near the vorticity minimum, thus creating HD instability given a sufficiently deep well. Again, the spectral results show the low-field MCI branch bifurcating and connecting to the $V_A/(r_1\Omega_0) = 0$ HD instability branch (Tanh3, Tanh4 in Fig. 20).

A consequence of bifurcation is that in HD-MHD unstable flows, the low-field MCI modes will tend to be resonance localized, inheriting the localization properties of the HD mode to which it connects. This is because hydrodynamic modes are localized about the Corotation point (the point in the regime where $\bar{\omega} = 0$) (see inset of Fig. 20c). In the absence of magnetic fields, there are no Alfvénic resonances. Since the resonance condition is continuous, the resonances must bifurcate from the Corotation point as the magnetic field strength becomes non-zero. We will utilize this bifurcation argument in Section V B 3 to provide a tool to calculate MHD onset in the presence of HD instability. We can observe such a resonance localized MCI mode illustrated in the inset figure of Figure 19c.

3. *MHD Onset - Critical Rm*

The critical parameters (e.g., minimum Rm and V_A) for the onset of MHD instability depend on the background flow configuration. Using the spectral diagram method (see Sec. V A 1), we compare the instability boundaries at low Rm for the Keplerian flow versus the Exp3 profile (Fig. 21). While both profiles are hydrodynamically stable and exhibit non-axisymmetric onset via a global MCI mode, the location and shape of the onset boundary in the (Rm-V_A) plane differ significantly, underscoring the sensitivity of the instability domains to flow configuration. Moreover, it's important to note that the significantly lower onset Rm exhibited by the Exp3

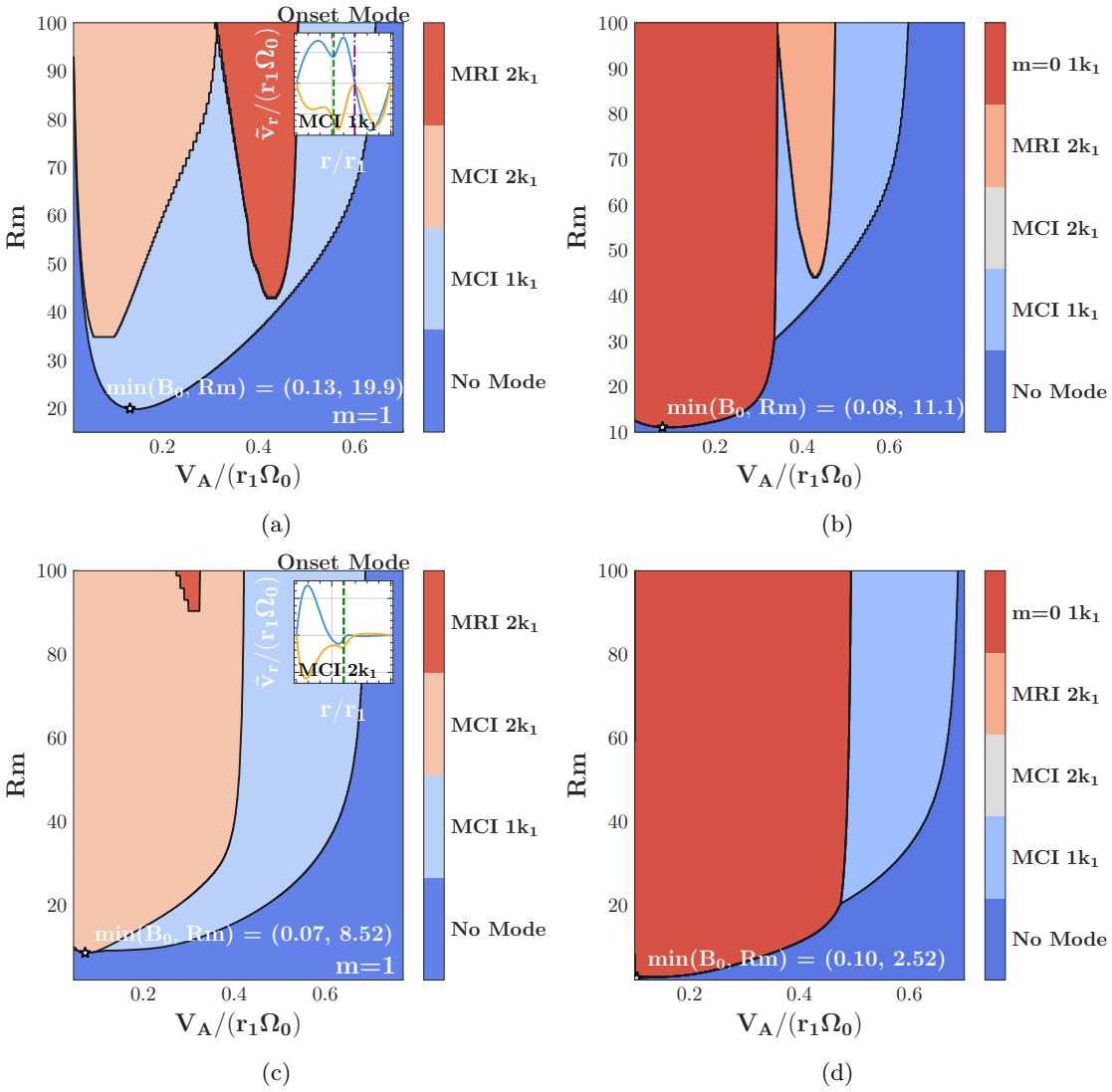

FIG. 21: Vertical field dominant mode instability boundaries and onset parameters are shown to heavily depend on flow configuration. We demonstrate dominant modes at low Rm for Kep (a,b) and Exp3 ((c,d), see Fig. 15 for the flow configuration definition) via the global resistive shooting method (as denoted in the color bar). In (a,c) we only consider non-axisymmetric ($m = 1$), whereas in (b,d) we compare the dominant non-axisymmetric ($m = 1$) modes with the $m = 0$ $1k_1$ mode at $r_1k_1 = \pi/4$, $k_r^2(r) =$ MWKB, and $r_2 - r_1 = 4r_1$ (AR1). In (a,c), we show that at low Rm, only low k_z ($\leq 2k_1$) MRI and MCI modes are unstable. Whereas in (b,d), we demonstrate that the $m = 0$ mode is dominant for low magnetic fields over all non-axisymmetric modes, but the MCI $1k_1$ mode remains dominant at large magnetic fields. Shooting is performed for $\mathrm{Pm} = 10^{-6}$. Insets demonstrate that the non-axisymmetric onset of instability occurs at a global MCI mode.

profile can be attributed to the underlying curvature of the profile, as the Keplerian and Exp3 profiles are actually very close in structure (see Fig. 10). In fact, a power-law fit of the Exp3, actually yields a profile with very similar shear to that of Keplerian, and thus the difference in the behaviors exhibited by the profiles can be attributed primarily to curvature.

Moreover, Figure 21 provides insights into experimentally testable regimes as it utilizes both a low viscosity ($\mathrm{Pm} = 10^{-6}$) and exhibits a flow profile similar to that observed from non-linear simulations [10, 20, 33]. Importantly, the axisymmetric and non-axisymmetric onsets predicted via the spectral diagram method closely match those observed in recent simulations [20]. Further refinement of input parameters, including matching of boundary conditions, aspect ratio, and direct input of steady-state flow configuration, can be utilized to reproduce the observed onset behavior in recent works fully. This analysis, however, demonstrates that, among perturbations of flow configuration, studying both the ax-

isymmetric ($m = 0$) $1k_1$ and MCI modes is required to define the behavior near instability onset. In particular, while the $m = 0$ $1k_1$ mode remains dominant near low magnetic fields, the MCI $1k_1$ mode almost exclusively defines the high-field behavior of the system.

Meanwhile, in flows that are already hydrodynamically unstable (when $V_A = 0$, $\gamma > 0$), the concept of MHD onset requires careful definition. As shown in Sec. V B 2, the MCI mode bifurcates into an HD branch as magnetic fields vanish. We propose viewing the emergence of MHD-HD dynamics as a bifurcation process of the Alfvénic resonances about the Corotation point. Since the Corotation point is a solution to the field-less resonance condition (Eq. 10 with the real component of the right hand side zero), it must also be a solution to the finite-field resonance condition if there is no real component on the right hand side. Specifically, this occurs when the roots of the resonance condition are degenerate, such that:

$$\mathrm{Re}\left(\sqrt{4\omega_A^2 - (\eta-\nu)^2 Q^2}\right) = 0$$

This condition then gives a set of transition parameters η, ν at a finite field where the system will transition from degenerate roots (Corotation point only) to two solutions (Alfvénic resonances).

However, as Q^2 and ω_A^2 are radially varying quantities, we must estimate the radial location where the resonance condition must degenerate. Since We estimate this location as the Corotation point $r_c \equiv \{r \in [r_1, r_2] \,|\, \omega_r - m\Omega(r) = 0\}$, as the Alfvénic resonances converge about r_c. Without this choice, the onset criterion would be a flow and ideal MHD mode independent quantity (ω_r). We know, however, from simulations [20] and Section V B 3 that MHD onset is intrinsically a flow-dependent parameter. Thus, the choice of r_c is fitting to evaluate the MHD onset, such that the onset criterion can be estimated as,

$$\mathrm{Rm}_H = \frac{(1-\mathrm{Pm})\left(k_r^2(r_c) + m^2/r_c^2 + k_z^2\right)}{2\omega_A(r_c)}. \qquad (19)$$

Figure 22 illustrates the bifurcation process for the HD-unstable Exp5 profile from direct global shooting. As Rm decreases towards the onset value found via shooting (Rm $\approx$ 11.3), the Alfvénic resonances are shown to merge on the Corotation point r_c. The predicted onset from Eq. 19 using the ideal frequency is $\mathrm{Rm}_H \approx 12.4$, in reasonable agreement. The discrepancy arises from the shift in ω_r (and thus r_c) between the ideal limit and the onset point, though iteration via shooting could improve this prediction. This analysis provides a useful method for estimating MHD onset thresholds in the presence of HD instability, linking it directly to the fundamental resonance structure. Developing analogous resonance-based onset criteria for HD-stable flows remains an area of future investigation.

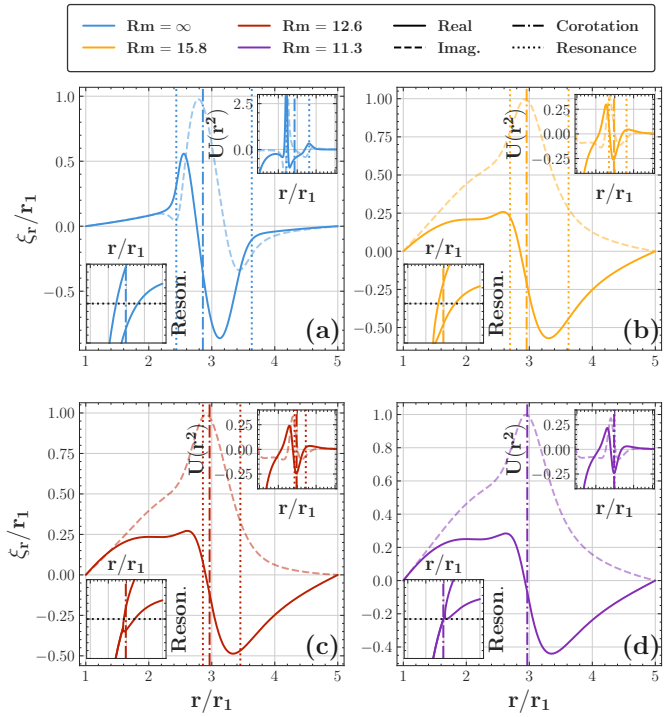

FIG. 22: Vertical field shooting resonances for the Exp5 configuration show the onset of the MHD mode (MCI) as Rm is increased (with the onset Rm = 11.3). Four resistivities are chosen to demonstrate that the Alfvénic resonances bifurcate from the Corotation point, with (a) Rm = ∞ (no viscosity), (b) Rm = 15.8, (c) Rm = 12.6, and (d) Rm = 11.3 at Pm = 0. The upper right inset plots show that the potentials move from those destabilized by the Alfvénic resonances to a well about the Corotation point. The lower left inset plots show the resonance condition (see Eq. 10), plotting both branches and resonances attributed to the equation's roots. Equation 19 predicts an onset at $\mathrm{Rm}_H = 12.4$, whereas an onset at Rm = 11.3 is observed via shooting. All shooting was performed for the $k_z = 1k_1$ ($r_1 k_1 = \pi/4$) non-axisymmetric ($m = 1$) MCI mode at $V_A/(r_1\Omega_0) = 0.1$.

C. Disk Configuration and spatial curvature

The geometry of the differentially rotating plasma significantly influences MHD mode stability. This has already been hinted at in Section V B 1, which established that vorticity gradients Γ' are intrinsically linked to the curvature of the flow profile (and hence the domain). Here, we investigate the distinct effects of the physical boundaries and dimensions, specifically the global curvature (related to r_2/r_1), the radial aspect ratio ($r_1/(r_2 - r_1)$), and the vertical aspect ratio ($\Delta z/\Delta r$). Increased geometric curvature strongly favors the Magneto-Curvature instability, reinforcing its characterization as a "curvature mode," while the MRI is less sensitive to global curvature. Furthermore, we will demonstrate MCI

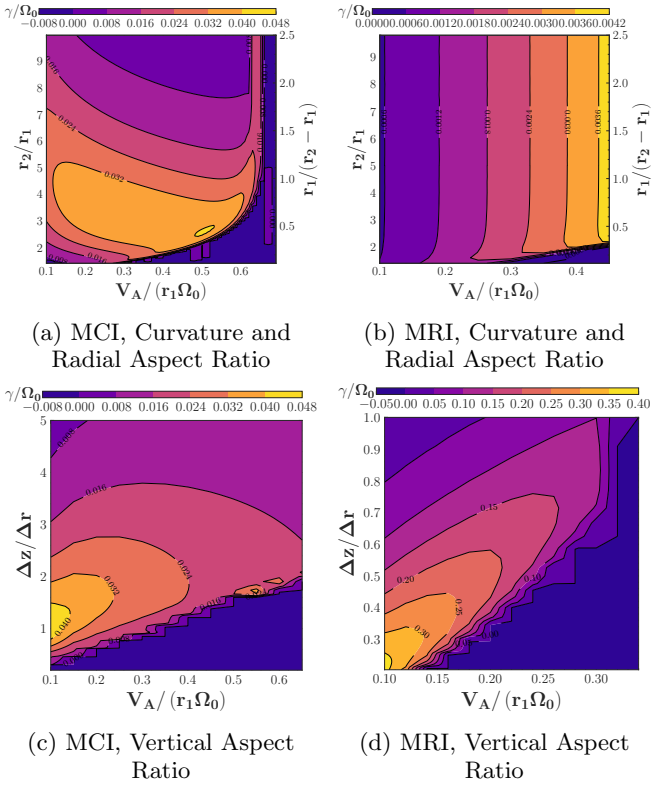

(a) MCI, Curvature and Radial Aspect Ratio

(b) MRI, Curvature and Radial Aspect Ratio

(c) MCI, Vertical Aspect Ratio

(d) MRI, Vertical Aspect Ratio

FIG. 23: Growth rates of non-axisymmetric ($m = 1$) modes (MCI (a,c), MRI (b,d)) as disk configuration is varied from the ideal global shooting method with the Keplerian flow configuration. In (a,b), we vary disk curvature and radial aspect ratio by tuning r_2/r_1 and $r_1/(r_2 - r_1)$, respectively, for $k_z/k_1 = 1$. As disk curvature increases ($r_2/r_1 \to 1$), the MCI mode becomes increasingly dominant and vice versa. In contrast, curvature has little effect on the growth rates of the MRI mode. In (c,d) we vary the vertical aspect ratio by tuning $\Delta z/\Delta r$ ($r_2/r_1 = 5$). We find MCI modes dominate in intermediate thickness ($\Delta z/\Delta r \sim 1$), whereas MRI dominates in thin disks ($\Delta z/\Delta r \ll 1$).

dominates in vertically moderate disks ($\Delta z/\Delta r \sim 1$), whereas MRI prevails in thin disks ($\Delta z/\Delta r \ll 1$). We explore these dependencies using the ideal global shooting method with a Keplerian profile ($\Omega(r) \propto 1/r^{3/2}$) and a purely vertical magnetic field, varying one geometric parameter at a time for MRI and MCI individually (see Fig. 23). We vary the vertical aspect ratio, the radial aspect ratio, and the curvature for this span while keeping the inner radius fixed.

First, we vary the ratio r_2/r_1 (implicitly varying the radial aspect ratio as well), effectively changing the global curvature (Figs. 23a,b). As r_2/r_1 decreases towards 1 (increasing curvature), the MCI growth rates significantly increase, dominating over MRI. This supports the notion that geometric curvature provides free energy for the MCI. At very high curvature (r_2/r_1 very close to 1), MCI growth rates decrease, potentially due to boundary effects or reduced radial variation limiting access to flow energy. At low curvature, MCI modes approach stability ($r_2/r_1 \to \infty$, which corroborates the expectation that MCI vanish in the Cartesian limit. In contrast, the MRI growth rates show only a weak dependence on r_2/r_1, consistent with its more localized nature.

Next, we vary radial aspect ratio (Figs. 23c,d). Smaller radial aspect ratios (larger radial gaps) generally allow modes access to a larger reservoir of free energy from the mean flow shear. Accordingly, MRI and MCI growth rates tend to increase with radial aspect ratio. However, unlike MRI, which uniformly favors smaller aspect ratios, MCI is also dominant for larger radial aspect ratios. This is because varying radial aspect ratio, while keeping r_1 fixed, also intrinsically varies spatial curvature. Thus, sufficiently small radial aspect ratios destabilize the MCI as curvature vanishes. Therefore, MCI dominates for intermediate radial aspect ratios, as there is a tradeoff between energy from curvature effects and accessing the energy from the mean flows.

Finally, we investigate the effect of vertical aspect ratio ($\Delta z/\Delta r$) for both MRI and MCI modes (see Figs. 23e,f) by varying z_2, z_1 while keeping r_1, r_2 fixed. We find that MRI is uniformly preferred in thinner disks ($\Delta z/\Delta r \ll 1$). In contrast, MCI is preferred in intermediate vertical aspect ratio disks ($\Delta z/\Delta r \sim 1$), while being stabilized for sufficiently thick disks ($\Delta z/\Delta r \gg 1$).

These ideal MHD results suggest that MCI is most dominant in geometrically moderately thick, highly curved domains with an intermediate radial aspect ratio (intermediate radial gap). Conversely, MRI is favored in thin, less curved domains with a small radial aspect ratio (large radial gap).

We corroborate these spectral results via a sweep of linear NIMROD simulations for two additional radial aspect ratios (AR0 & AR2 with a purely azimuthal magnetic field. Figure 24 compares growth rates from NIMROD with corresponding ideal shooting results (using dominant k_z observed in NIMROD). Despite the change to an azimuthal field, we demonstrate that these scaling trends hold at finite resistivity: the high-curvature AR0 geometry shows MCI dominance across the entire range of V_A simulated, while the low-curvature AR2 geometry exhibits a transition from MRI to MCI dominance at a significantly higher V_A compared to the intermediate radial aspect ratio AR1 case (cf. Fig. 24). This confirms that increased geometric curvature robustly promotes MCI dominance.

These findings have important implications for laboratory experiments, which typically operate in high curvature, intermediate radial aspect ratio, and moderate vertical aspect ratio regimes. PPPL's MRI experiment, for example, operates in a regime with $r_2/r_1 = 3$, $r_1/(r_2 - r_1) = 1/2$, and $\Delta z/\Delta r = 2$ ([10], [33], [20]). Our analysis indicates that such parameters strongly favor the MCI (low-frequency branch of non-axisymmetric modes) as the dominant instability, especially at moderate to strong magnetic fields. Observing MRI (high frequency

localized branch) in such configurations might require accessing regimes of very high magnetic Reynolds number (Rm) at low magnetic field strengths, where MRI growth rates might exceed those of MCI. Identifying transitions between MCI and MRI could be achieved by observing discontinuous changes in the dominant mode frequency, provided the target mode (e.g., MRI) has a sufficiently large ideal growth rate in the relevant parameter space to overcome damping and competing modes. Spectral diagrams, as constructed in Section V A 1, can help delineate the parameter regimes where different modes are expected to dominate.

VI. SUMMARY AND CONCLUSIONS

Understanding the linear stability of differentially rotating magnetized disks is crucial for explaining the drivers of turbulence and angular momentum transport in systems like accretion disks. We investigated the global linear dynamics of non-axisymmetric ($m = 1$) MHD instabilities in such disks, threaded with vertical or azimuthal magnetic fields, exploring the dependence on diffusivity, flow configuration, and disk geometry. Utilizing a combination of local WKB analysis, a non-ideal global spectral method (solved via shooting), and linear initial-value simulations (NIMROD), we established that the two primary $m = 1$ non-axisymmetric modes–the Magneto-Rotational Instability (MRI) and the Magneto-Curvature Instability (MCI)–dominate in different regimes of parameter space due to their distinct mode characteristics (structure, frequency, and configuration sensitivity). MRI modes are typically high-frequency, localized radially and vertically (high k_z), whereas MCI modes are low-frequency, global, and have low k_z. A key finding is that at low magnetic Reynolds number (Rm), the global structure of MCI allows it to persist. At the same time, MRI is preferentially stabilized due to the broadening of its structure around its Alfvénic resonances (see Fig. 6). Consequently, we argue that in disks with finite curvature, the onset of MHD instability typically occurs via the global MCI $1k_1$ mode (e.g., Fig. 13), consistent with recent simulation results showing onset via a global low-frequency mode [20]. The detailed dependence of this stability landscape, including onset conditions and mode competition, on flow profiles, field structure, and disk geometry was systematically explored using these methods and is summarized below.

Our analysis began with a local WKB approach (Sec. III), which indicated that non-ideal effects shift dominant instabilities towards larger spatial scales (lower k_z, k_r, $m = 1$) compared to the ideal limit. Recognizing the limitations of local analysis, we developed a non-ideal global stability method (Sec. IV). This involved deriving a 1D second-order ordinary differential equation (ODE) governing the radial mode structure by applying a targeted approximation to the diffusive terms [29], solved via shooting to find the eigenvalues and eigenfunctions. To understand free energy contributions, we extended the effective potential formalism [23] to the non-ideal regime, revealing that diffusion broadens the potential structure around Alfvénic resonances (Sec. IV D, Fig. 6). This broadening preferentially stabilizes the localized MRI, explaining the persistence of the global MCI at lower Rm.

The global spectral method was validated against linear initial-value NIMROD simulations (Sec. V A). The MWKB ("Modified WKB") and TWKB ("Traditional WKB") approximations for the diffusive terms yielded reasonable agreement with NIMROD growth rates across various parameters, particularly capturing onset trends, stability boundaries, and mode characteristics (mode structure, frequencies, etc) despite some differences in growth rates when MCI is most global (Sec. IV A, Figs. 4,12, and 13 (insets)). Leveraging the efficiency of the spectral method, we introduced *spectral diagrams* (Sec. V A 1), which map the dominant instability (largest growth rate) (MCI or MRI with specific k_z) across parameter space (e.g., Rm vs. V_A, Figs. 13/21). These diagrams successfully delineated regions of mode dominance consistent with NIMROD simulations and provide a valuable tool for predicting instability boundaries, onset parameters, and observable characteristics like mode frequency or growth rate. Notably, they predict distinct frequency shifts associated with the transition between instability branches (MRI to MCI and vice versa).

Systematic parameter scans and analysis of the effective potential formalism (see reformulation in Eq. 16) were conducted to clarify the influence of flow configuration–specifically vorticity $\Gamma(= \Omega(2-q))$, its radial gradient Γ', and relative flow curvature $\langle\Gamma'\rangle_r / \langle\Gamma\rangle_r$–on MHD stability (Sec. V B). Particular emphasis was placed on studying flow characteristics through the lens of vorticity, as it provides a physically motivated description of the competition between flow curvature (2Ω) and shear ($-q\Omega$). We then argue that $\langle\Gamma'\rangle_r / \langle\Gamma\rangle_r$ (for $\langle.\rangle_r$ the radial average) provides a normalized measure of whether a flow is shear-dominated or curvature-dominated, and thus define this as relative flow curvature. Utilizing this framework, both MRI and MCI exhibit complex dependency on vorticity (Γ) and its gradient (Γ'), as suggested by a heuristic analysis of the potential terms (summarized in Table II and demonstrated in Figure 17). At low field strengths ($\omega_A^2 \ll \bar{\omega}^2$), vorticity ($\Gamma$ terms) tends to stabilize MCI while destabilizing MRI; concurrently, vorticity gradients (Γ' term) act to destabilize the MRI and confine the MCI. At intermediate field strengths ($\omega_A^2 \sim \bar{\omega}^2$), both vorticity and its gradient generally act to destabilize both modes. At high field strengths ($\omega_A^2 \gg \bar{\omega}^2$), vorticity tends to destabilize MCI while confining MRI; conversely, vorticity gradients tend to stabilize MCI while destabilizing MRI. These complex, field-dependent interactions underscore the sensitivity of mode competition and stability to the detailed structure of the flow profile beyond simple shear parameters.

We perform spectral scans over profiles with non-

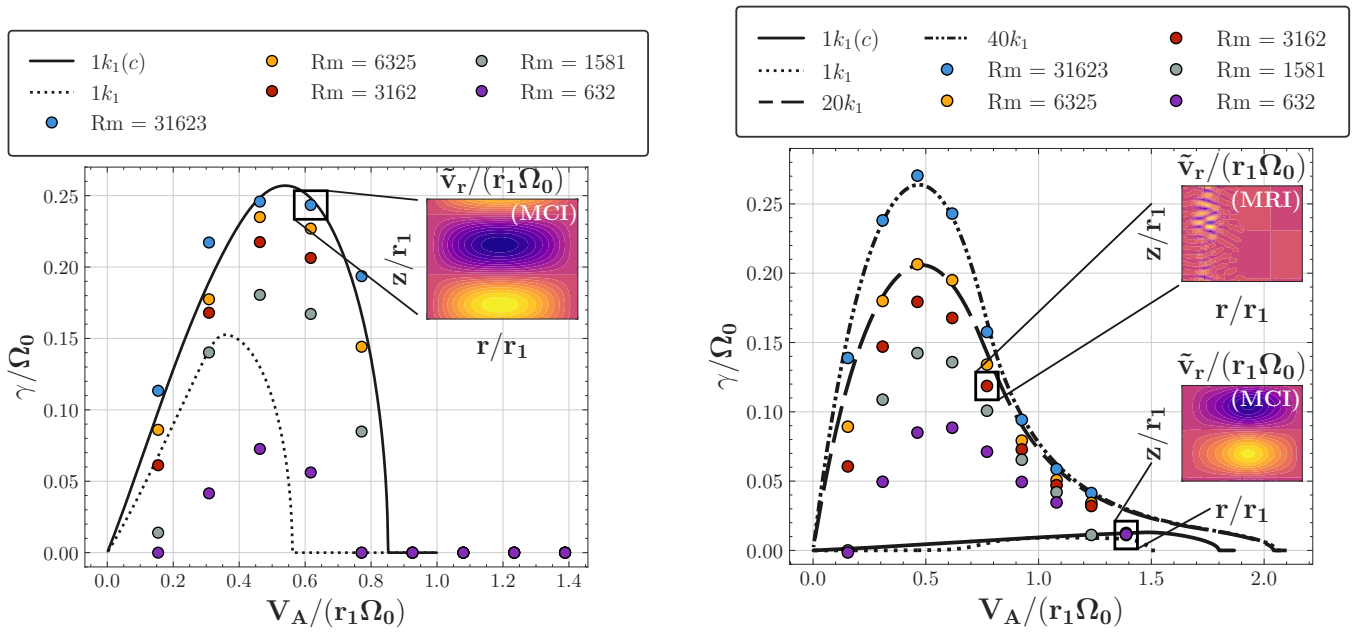

(a) (b)

FIG. 24: Azimuthal field growth rates from both NIMROD simulations (all finite Rm points) and the ideal global shooting method for the AR0 radial aspect ratio (a) and the AR2 radial aspect ratio (b). The AR0 radial aspect ratio has the global $1k_1$ MCI mode dominant for the entire regime due to the increased curvature of the domain. Conversely, the AR2 radial aspect ratio has the MRI mode dominant for more of the regime than previous simulations (AR1, see Fig. 11) due to decreased curvature. Wave numbers (k_z) for shooting curves were determined by looking at the mode structure from NIMROD, but do not capture all observed wave numbers for MRI. Inset figures show mode structures from NIMROD simulations. Finally, definitions for the AR0, AR2 radial aspect ratios are given in Figure 9.

uniform $q(r)$ (Exponential configuration, defined in Fig. 15) and uniform $q(r)$ (power-law profiles), finding that the observed scaling generally matches our heuristic analysis (see Fig. 18). In this figure, it is also apparent that MCI modes with non-uniform $q(r)$ appear more resilient under perturbation of flow characteristics compared to the uniform $q(r)$ profiles, likely due to additional free energy contributions [23] associated with vorticity gradients (Γ'), and thus flow curvature, when $q' \neq 0$ (c.f. 15a,b,e,f). Meanwhile, MRI modes remain agnostic to the underlying uniformity (and resultant curvature) of the profile, which is consistent with their local nature (c.f. 15c,d,g,h). This reinforces the conclusion that the MCI is a curvature-driven instability, and implies that flow configurations with larger curvature will experience onset of instability at lower Rm. This difference in curvature can be observed directly through flows with similar q, but different vorticities, where even a small perturbation in the profile results in a significant change in the onset parameters (see Fig. 21).

We also explored the interaction with hydrodynamic (HD) instability (Sec. V B 2), finding that the MCI branch typically bifurcates into an HD mode at low magnetic fields when the flow is HD unstable (see Fig. 19). This includes non-axisymmetric HD instability driven by vorticity wells, even for flows stable by the axisymmetric Rayleigh criterion ($q(r) < 2$) (see Fig. 20). Through the vorticity framework, analysis of mode confinement yields a physically motivated picture: vorticity wells provide confinement (stability), and vorticity gradients act as a restoring (and thus confining) force within these wells. This same argument demonstrates that hydrodynamic instability is unlikely to occur in flow configurations with low flow curvature ($q' = 0$), and that sufficiently deep vorticity wells can confine hydrodynamic perturbations for $q < 2$. At finite fields, these hybrid HD-MCI modes exhibit a superposition of both global MCI and Corotation localized (points where the Doppler shifted frequency equals zero) mode structure (see Fig. 19), leading to resonance-localized MCI modes as field strength increases. As Alfvénic resonances must vanish in the absence of magnetic fields, we argue that MHD onset can be viewed as a bifurcation process of the resonances about the Corotation point as magnetic Reynolds number (Rm) increases. With this perspective, we provide a criterion to estimate the magnetic Reynolds number (Rm) threshold for MHD onset in the presence of HD instability (Eq. 19) and demonstrate the bifurcation process (see Fig. 22), finding reasonable agreement with the theoretical estimate.

Disk geometry was also found to be critical (Sec. V C). MRI modes dominate in thin disks ($\Delta z/\Delta r \ll 1$) with low global curvature ($r_2/r_1 \gg 1$) and small radial aspect ratio (large radial gaps). In contrast, MCI modes dominate in disks with moderate vertical aspect ratio ($\Delta z/\Delta r < 1$, global curvature ($r_2/r_1 \sim 1$), and radial aspect ratio (Fig. 23). This trend was qualitatively confirmed by NIMROD simulations in different radial aspect ratio geometries with azimuthal fields (Fig. 24). These findings suggest that MCI likely dominates typical laboratory experiments operating in highly curved, moderately thick domains.

While this paper utilized maximally diffusive regimes (Pm = 1) to benchmark the extended global shooting method, we also demonstrate behavior at low and intermediate viscosities (see Figures 14 and 21). The latter classifications are significant, as they encompass experimentally testable regimes (Pm = 10^{-6}), demonstrating that the $m = 0$ and $m = 1$ MCI $1k_1$ modes each have their own distinct regimes of dominance. These diagrams reaffirm the importance of studying non-axisymmetric modes in these regimes, particularly in the strong field limit. Moreover, we demonstrate that these observations hold even in profiles close to those used experimentally (see Fig. 21, [10, 20, 33]). In addition, due to the inherent modularity of this method, further refinement of exploration remains open and a topic for future inquiry such as direct input of the nonlinearly simulated steady-state flows.

While the resistive approximations have quantitative limitations, this work demonstrates they capture essential scaling behaviors and mode properties, providing a computationally efficient tool for exploring parameter space and guiding simulations or experiments. Methods for refining these approximations remain a path for future research. Given the successful application to resistive MHD, extending these spectral and potential methods to incorporate additional physics, such as Hall MHD effects, which are significant in specific plasma regimes, represents another promising direction. Similarly, applying these efficient tools to analyze stability in more complex, non-uniform flow profiles, such as those exhibiting vorticity minima [20], is warranted. This linear stability analysis provides a foundation for future studies focusing on the non-linear evolution, turbulence, and associated transport driven by these instabilities.

ACKNOWLEDGMENTS

The authors thank Matthew Pharr, Yin Wang, Hantao Ji, Jeremy Goodman, and Erik Gilson for insightful discussions. Simulations were performed on the cluster at the Princeton Plasma Physics Laboratory. Full simulation data is available on the Princeton Plasma Physics Laboratory Cluster, and more concisely available on GitHub [34]. This work was supported by the National Science Foundation under Award No. NSF 2308839 and DOE under Grant No. DE-AC02-09CH11466.

[1] N. Shakura and R. Sunyaev, Astronomy and Astrophysics, **Vol. 24**, p. 337 (1973).

[2] L. Salas, G. Musoke, K. Chatterjee, S. Markoff, O. Porth, M. Liska, and B. Ripperda, Resolution analysis of magnetically arrested disk simulations (2024), arXiv:2405.00564 [astro-ph].

[3] E. P. Velikhov, Soviet Physics JETP **36 (9), NUMBER 5** (1959).

[4] S. Chandrasekhar, *Hydrodynamic and hydromagnetic stability*, dover ed ed. (Dover Publications, New York, 1981).

[5] S. A. Balbus and J. F. Hawley, The Astrophysical Journal **376**, 214 (1991), aDS Bibcode: 1991ApJ...376..214B.

[6] The Event Horizon Telescope Collaboration, K. Akiyama, A. Alberdi, W. Alef, J. C. Algaba, R. Anantua, K. Asada, R. Azulay, U. Bach, A.-K. Baczko, D. Ball, M. Baloković, B. Bandyopadhyay, J. Barrett, M. Bauböck, B. A. Benson, D. Bintley, L. Blackburn, R. Blundell, K. L. Bouman, G. C. Bower, H. Boyce, M. Bremer, R. Brissenden, S. Britzen, A. E. Broderick, D. Broguiere, T. Bronzwaer, S. Bustamante, J. E. Carlstrom, A. Chael, C.-k. Chan, D. O. Chang, K. Chatterjee, S. Chatterjee, M.-T. Chen, Y. Chen, X. Cheng, I. Cho, P. Christian, N. S. Conroy, J. E. Conway, T. M. Crawford, G. B. Crew, A. Cruz-Osorio, Y. Cui, R. Dahale, J. Davelaar, M. De Laurentis, R. Deane, J. Dempsey, G. Desvignes, J. Dexter, V. Dhruv, I. K. Dihingia, S. S. Doeleman, S. A. Dzib, R. P. Eatough, R. Emami, H. Falcke, J. Farah, V. L. Fish, E. Fomalont, H. A. Ford, M. Foschi, R. Fraga-Encinas, W. T. Freeman, P. Friberg, C. M. Fromm, A. Fuentes, P. Galison, C. F. Gammie, R. García, O. Gentaz, B. Georgiev, C. Goddi, R. Gold, A. I. Gómez-Ruiz, J. L. Gómez, M. Gu, M. Gurwell, K. Hada, D. Haggard, R. Hesper, D. Heumann, L. C. Ho, P. Ho, M. Honma, C.-W. L. Huang, L. Huang, D. H. Hughes, S. Ikeda, C. M. Violette Impellizzeri, M. Inoue, S. Issaoun, D. J. James, B. T. Jannuzi, M. Janssen, B. Jeter, W. Jiang, A. Jiménez-Rosales, M. D. Johnson, S. Jorstad, A. C. Jones, A. V. Joshi, T. Jung, R. Karuppusamy, T. Kawashima, G. K. Keating, M. Kettenis, D.-J. Kim, J.-Y. Kim, J. Kim, J. Kim, M. Kino, J. Y. Koay, P. Kocherlakota, Y. Kofuji, P. M. Koch, S. Koyama, C. Kramer, J. A. Kramer, M. Kramer, T. P. Krichbaum, C.-Y. Kuo, N. La Bella, S.-S. Lee, A. Levis, Z. Li, R. Lico, G. Lindahl, M. Lindqvist, M. Lisakov, J. Liu, K. Liu, E. Liuzzo, W.-P. Lo, A. P. Lobanov, L. Loinard, C. J. Lonsdale, A. E. Lowitz, R.-S. Lu, N. R. MacDonald, J. Mao, N. Marchili, S. Markoff, D. P. Marrone, A. P. Marscher, I. Martí-Vidal, S. Matsushita, L. D. Matthews, L. Medeiros, K. M. Menten, I. Mizuno, Y. Mizuno, J. Montgomery, J. M. Moran, K. Moriyama,

M. Moscibrodzka, W. Mulaudzi, C. Müller, H. Müller, A. Mus, G. Musoke, I. Myserlis, H. Nagai, N. M. Nagar, M. Nakamura, G. Narayanan, I. Natarajan, A. Nathanail, S. N. Fuentes, J. Neilsen, C. Ni, M. A. Nowak, J. Oh, H. Okino, H. Olivares, T. Oyama, F. Özel, D. C. M. Palumbo, G. F. Paraschos, J. Park, H. Parsons, N. Patel, U.-L. Pen, D. W. Pesce, V. Piétu, A. Popstefanija, O. Porth, B. Prather, D. Psaltis, H.-Y. Pu, V. Ramakrishnan, R. Rao, M. G. Rawlings, A. W. Raymond, L. Rezzolla, A. Ricarte, B. Ripperda, F. Roelofs, C. Romero-Cañizales, E. Ros, A. Roshanineshat, H. Rottmann, A. L. Roy, I. Ruiz, C. Ruszczyk, K. L. J. Rygl, S. Sánchez, D. Sánchez-Argüelles, M. Sánchez-Portal, M. Sasada, K. Satapathy, T. Savolainen, F. P. Schloerb, J. Schonfeld, K.-F. Schuster, L. Shao, Z. Shen, D. Small, B. W. Sohn, J. SooHoo, L. D. S. Salas, K. Souccar, J. S. Stanway, H. Sun, F. Tazaki, A. J. Tetarenko, P. Tiede, R. P. J. Tilanus, M. Titus, K. Toma, P. Torne, T. Toscano, E. Traianou, T. Trent, S. Trippe, M. Turk, I. Van Bemmel, H. J. Van Langevelde, D. R. Van Rossum, J. Vos, J. Wagner, D. Ward-Thompson, J. Wardle, J. E. Washington, J. Weintroub, R. Wharton, M. Wielgus, K. Wiik, G. Witzel, M. F. Wondrak, G. N. Wong, Q. Wu, N. Yadlapalli, P. Yamaguchi, A. Yfantis, D. Yoon, A. Young, Z. Younsi, W. Yu, F. Yuan, Y.-F. Yuan, J. Anton Zensus, S. Zhang, G.-Y. Zhao, S.-S. Zhao, A. Allardi, S.-H. Chang, C.-C. Chang, S.-C. Chang, C.-C. Chen, R. Chilson, A. Faber, D. M. Gale, C.-C. Han, K.-C. Han, Y. Hasegawa, J. L. Hernández-Rebollar, Y.-D. Huang, H. Jiang, H. Jinchi, K. Kimura, D. Kubo, C.-T. Li, L. C.-C. Lin, C.-T. Liu, K.-Y. Liu, L.-M. Lu, P. Martin-Cocher, Z. Meyer-Zhao, A. Montaña, A. Moraghan, M. E. Moreno-Nolasco, H. Nishioka, T. J. Norton, G. Nystrom, H. Ogawa, P. Oshiro, N. Pradel, G. Principe, P. Raffin, I. Rodríguez-Montoya, P. Shaw, W. Snow, T. K. Sridharan, R. Srinivasan, T.-S. Wei, and C.-Y. Yu, Astronomy & Astrophysics **681**, A79 (2024).

[7] J. Goodman and H. Ji, Journal of Fluid Mechanics **462**, 365 (2002).

[8] D. R. Sisan, N. Mujica, W. A. Tillotson, Y.-M. Huang, W. Dorland, A. B. Hassam, T. M. Antonsen, and D. P. Lathrop, Physical Review Letters **93**, 114502 (2004).

[9] X. Wei, H. Ji, J. Goodman, F. Ebrahimi, E. Gilson, F. Jenko, and K. Lackner, Physical Review E **94**, 063107 (2016).

[10] Y. Wang, E. P. Gilson, F. Ebrahimi, J. Goodman, K. J. Caspary, H. W. Winarto, and H. Ji, Nature Communications **13**, 4679 (2022), arXiv:2209.08410 [astro-ph, physics:physics].

[11] J. F. Hawley, C. F. Gammie, and S. A. Balbus, The Astrophysical Journal **440**, 742 (1995), aDS Bibcode: 1995ApJ...440..742H.

[12] J. M. Stone, J. F. Hawley, C. F. Gammie, and S. A. Balbus, The Astrophysical Journal **463**, 656 (1996), aDS Bibcode: 1996ApJ...463..656S.

[13] S. Fromang, J. Papaloizou, G. Lesur, and T. Heinemann, Astronomy & Astrophysics **476**, 1123 (2007), arXiv:0705.3622 [astro-ph].

[14] M. E. Pessah, C.-k. Chan, and D. Psaltis, The Astrophysical Journal **668**, L51 (2007).

[15] G. Bodo, A. Mignone, F. Cattaneo, P. Rossi, and A. Ferrari, Astronomy & Astrophysics **487**, 1 (2008).

[16] M. Machida, M. R. Hayashi, and R. Matsumoto, The Astrophysical Journal **532**, L67 (2000).

[17] J. F. Hawley, The Astrophysical Journal **528**, 462 (2000).

[18] A. Mishra, G. Mamatsashvili, and F. Stefani, Physical Review Fluids **7**, 064802 (2022).

[19] F. Ebrahimi and M. Pharr, The Astrophysical Journal **936**, 145 (2022).

[20] Y. Wang, F. Ebrahimi, H. Lu, J. Goodman, E. P. Gilson, and H. Ji, Physical Review Letters **134**, 135101 (2025).

[21] A. Mishra, G. Mamatsashvili, and F. Stefani, Physical Review Fluids **9**, 033904 (2024).

[22] A. Mishra, G. Mamatsashvili, and F. Stefani, Physical Review Fluids **8**, 083902 (2023).

[23] F. Ebrahimi and A. Haywood, Physics of Plasmas **32**, 030702 (2025).

[24] R. Matsumoto and T. Tajima, The Astrophysical Journal **445**, 767 (1995), aDS Bibcode: 1995ApJ...445..767M.

[25] G. I. Ogilvie and J. E. Pringle, Monthly Notices of the Royal Astronomical Society **279**, 152 (1996).

[26] R. Hollerbach, V. Teeluck, and G. Rüdiger, Physical Review Letters **104**, 044502 (2010).

[27] C. R. Sovinec, A. H. Glasser, T. A. Gianakon, D. C. Barnes, R. A. Nebel, S. E. Kruger, D. D. Schnack, S. J. Plimpton, A. Tarditi, and M. S. Chu, Journal of Computational Physics **195**, 355 (2004).

[28] F. Ebrahimi, B. Lefebvre, C. B. Forest, and A. Bhattacharjee, Physics of Plasmas **18**, 062904 (2011).

[29] R. Zou, J. Labarbe, Y. Fukumoto, and O. N. Kirillov, Physical Review E **101**, 013201 (2020), arXiv:1907.05488 [astro-ph, physics:physics].

[30] S. Chandrasekhar, in eng*Hydrodynamic and Hydromagnetic Stability*, Dover books on mathematics (Dover Publications, Inc, New York, 2013) pp. 382–427.

[31] C. Curry and R. E. Pudritz, Monthly Notices of the Royal Astronomical Society **281**, 119 (1996).

[32] J. Pino and S. Mahajan, The Astrophysical Journal **678**, 1223 (2008).

[33] Y. Wang, E. P. Gilson, F. Ebrahimi, J. Goodman, and H. Ji, Physical Review Letters **129**, 115001 (2022).

[34] A. Haywood and F. Ebrahimi, Nonideal stability analysis of differentially rotating plasmas with global curvature effects [Data set]. Zenodo. (2025).

Appendix A: Resistive MHD WKB Dispersion Relation

In Section III, we derived the non-ideal dispersion relation for non-axisymmetric MHD instabilities. This dispersion relation took the form:

$$\bar{\omega}^4 + C_3\bar{\omega}^3 + C_2\bar{\omega}^2 + C_1\bar{\omega} + C_0 = 0$$

Below, we define the coefficients C_3, C_2, C_1 and C_0:

$$C_3 = 2i\Omega\frac{\bar{k}_r k_\phi}{k^2} - \frac{i\kappa^2}{2\Omega}\frac{k_r k_\phi}{k^2} + \frac{i\bar{k}^2}{k^2}\left[(2\eta+\nu)\,k^2 + \nu k_z^2\right] + \frac{2\nu k_\phi^2\delta_c}{r^2k^2} \tag{A1}$$

$$C_2 = \frac{i\bar{k}_r k_\phi}{2k^2}\omega_A\omega_c\delta_c - \frac{1}{2}\left(\frac{k_z^2+k_\phi^2}{k^2}\right)\omega_c^2\delta_c - \kappa^2 - 2\omega_A^2 + \frac{ik_z^2 k_\phi\nu\delta_c}{rk^2}\left(\frac{\kappa^2}{\Omega}+4\Omega\right) - \frac{\bar{k}^2 k_\phi\eta}{k^2}\left(4\Omega\bar{k}_r - \frac{\kappa^2}{\Omega}k_r\right) + \frac{2ik_\phi\eta\delta_c}{r}\frac{\partial\Omega}{\partial\ln r}$$
$$+\left(\frac{4k_\phi^2\delta_c}{r^2} - \bar{k^4}\right)\left(\frac{k^2\eta^2 + k_z^2\nu^2}{k^2}\right) - \frac{2\eta\nu}{k^2}\left[\bar{k}^4\{k^2+k_z^2\} - \frac{2i\bar{k}^2k_\phi^2\delta_c}{r^2}\right] \tag{A2}$$

$$C_1 = \frac{1}{k^2}\left[\frac{ik_r k_\phi\kappa^2}{2\Omega} - 2i\bar{k}_r k_\phi - \frac{2\nu k_\phi^2\delta_c}{r^2} - i\bar{k}^2\left\{(2\eta+\nu)\left(\bar{k}_r k_r + k_\phi^2\right) + 2\left(\eta+\nu\right)k_z^2\right\}\right]\omega_A^2$$
$$+\frac{1}{k^2}\left[\frac{1}{2}\left\{\frac{\partial\Omega}{\partial\ln r} - 4\Omega\right\}\{k_z^2+k_\phi^2\} - k_z^2\frac{\kappa^2}{4\Omega} + \frac{ik_\phi}{r}\left\{2\eta\bar{k}_r k_r + \big(2\nu+3\eta\big)k_\phi^2 + 3\big(\nu+\eta\big)k_z^2 + ir\bar{k}^2\left(\frac{\eta\bar{k}_r}{2}+\nu k_r\right)\right\}\right]\omega_A\omega_c\delta_c$$
$$-\frac{i\bar{k}^2}{2k^2}\left[\eta k_\phi^2 + \{\eta+\nu\}k_z^2\right]\omega_c^2\delta_c - \frac{i}{k^2}\left[2\kappa^2\bar{k}^2k_z^2 + \left\{2\Omega\bar{k}_r k_\phi - \frac{\kappa^2}{2\Omega}k_r k_\phi\right\}\left\{\bar{k}^4\eta + \frac{2ik_\phi\delta_c}{r}\left(\frac{\partial\Omega}{\partial\ln r}+\frac{2ik_\phi\eta}{r}\right)\right\}\right]$$
$$+\frac{\eta\nu}{k^2}\left[\frac{4k_\phi^3\delta_c}{r^3}\left\{\frac{2\eta k_\phi}{r} - i\frac{\partial\Omega}{\partial\ln r}\right\} - \frac{2\eta\bar{k}^4k_\phi^2\delta_c}{r^2} - i\bar{k}^6\left\{\eta\bar{k}_r k_r + \eta k_\phi^2 + 2\left(\eta+\nu\right)k_\phi^2\right\} + \frac{2\bar{k}^2k_\phi\delta_c}{r}\left\{\left(\bar{k}_r k_r + k_\phi^2\right)\left(\frac{\partial\Omega}{\partial\ln r}+\frac{2i\eta k_\phi}{r}\right)\right.\right.$$
$$\left.\left.+2k_z^2\left(\frac{\partial\Omega}{\partial\ln r}+\frac{2i\left(\eta+\nu\right)k_\phi}{r} - 2\Omega - \frac{\kappa^2}{2\Omega}\right)\right\}\right] \tag{A3}$$

$$C_0 = \left[\omega_A^2 + \left\{\frac{k_\phi^2+k_z^2}{k^2}\right\}\frac{\partial\Omega^2}{\partial\ln r} + \frac{\bar{k}^2}{k^2}\left\{2\eta\Omega\bar{k}_r k_\phi - \left(\eta\frac{\kappa^2}{2\Omega} - \nu\frac{\partial\Omega}{\partial\ln r}\right)k_r k_\phi\right\}\right.$$
$$+\frac{ik_\phi\delta_c}{rk^2}\left\{\eta\left(\bar{k}_r k_r + k_z^2\right)\frac{\kappa^2}{\Omega} + \left(4\eta\Omega - 2\nu\frac{\partial\Omega}{\partial\ln r}\right)\left(k_\phi^2+k_z^2\right)\right\} + \frac{\eta\nu}{k^2}\left\{\left(k^2+k_z^2\right)\left(\bar{k}^4 + \frac{4k_\phi^2\delta_c}{r^2}\right) - \frac{4i\bar{k}^2k_\phi^2\delta_c}{r^2}\right\}\left.\right]\omega_A^2$$
$$+\left[\frac{4\eta\bar{k}_r k_\phi^2}{rk^2} + \frac{i\bar{k}^2}{2k^2}\left\{\eta\frac{\kappa^2}{2\Omega} + 4\eta\Omega\left(k_\phi^2+k_z^2\right) - \nu\frac{\partial\Omega}{\partial\ln r}\right\} + \frac{\eta\nu}{k^2}\left\{i\bar{k}^4k_r k_\phi + \frac{2i\bar{k}^2k_\phi}{r}\left(k^2+2k_z^2\right) - \frac{4i\bar{k}_r k_\phi^3}{r^2}\right\}\right]\omega_A\omega_c\delta_c \tag{A4}$$
$$+\frac{i\bar{k}_r k_\phi}{2k^2}\omega_A^3\omega_c\delta_c + \frac{\eta\nu\bar{k}^4}{2}\omega_c^2\delta_c + \frac{2i\eta k_\phi\delta_c\kappa^2}{r}\frac{\partial\Omega}{\partial\ln r} + \kappa^2\eta^2\left[\bar{k}^4 - \frac{4k_\phi^2\delta_c}{r^2}\right] + \eta\nu\left[\eta\bar{k}^4 + \frac{2ik_\phi\delta_c}{r}\frac{\partial\Omega}{\partial\ln r} - \frac{4\eta k_\phi^2\delta_c}{r^2}\right]$$
$$\times\left[\nu\bar{k}^4 - \frac{ik_\phi\delta_c}{r}\left\{\frac{\kappa^2}{\Omega}+4\Omega\right\} + \frac{4\nu k_\phi^2\delta_c}{r^2}\right]$$

Upon substitution of $k_r \to -ik_r$, this matches the previously known local dispersion relation for non-axisymmetric modes [19]. In the zero-curvature axisymmetric limit, $k_\phi, \delta_c \to 0$ and $\bar{k}_r \to k_r$, $\bar{k}^2 \to k^2$, this becomes the local dispersion relation for the axisymmetric MRI mode [5].

Appendix B: Convergence On Ideal MHD Limit

This section shows that Equation 6 converges on Equation 16 of [19] in the ideal limit. First, recall the 1D second-order equation boundary valued equation for $\xi_r(r)$, where $\xi_r(r) = -r\tilde{v}_r/(i\bar{\omega}_\eta)$:

$$\frac{d}{dr}\left(f\frac{d\xi_r}{dr}\right) + s\frac{d\xi_r}{dr} - g\xi_r = 0 \tag{B1}$$

where the coefficients f, s, and g are defined below. Taking the ideal limit, we note that much simplification can be done simply by taking $\bar{\omega}_\eta \to \bar{\omega}_\nu$.

$$f = \frac{r\left(\omega_A^2 - \bar{\omega}_\nu\bar{\omega}_\eta\right)}{k_z^2 r^2 + m^2}, \quad s = \underbrace{\frac{m(\bar{\omega}_\nu - \bar{\omega}_\eta)}{k_z^2 r^2 + m^2} r\Omega'}_{=0,\text{ since } \bar{\omega}_\eta \to \bar{\omega}_\nu},$$

$$g = \frac{\mathrm{d}}{\mathrm{dr}}\left\{\frac{m}{(k_z^2 r^2 + m^2)}\left[\underbrace{(\bar{\omega}_\eta - \bar{\omega}_\nu)\, r\Omega'}_{=0,\text{ since } \bar{\omega}_\eta \to \bar{\omega}_\nu} + (2\Omega\bar{\omega}_\eta + \omega_A\omega_c)\right]\right\}$$
$$+\frac{\left(\omega_A^2 + \omega_c^2 - \bar{\omega}_\nu\bar{\omega}_\eta\right)}{r} + \underbrace{\frac{\omega_s^2}{r}\left(\frac{\omega_A^2 - \frac{k_z^2 r^2 \bar{\omega}_\eta^2 + m^2\bar{\omega}_\eta\bar{\omega}_\nu}{k_z^2 r^2 + m^2}}{\omega_A^2 - \bar{\omega}_\nu\bar{\omega}_\eta}\right)}_{=\frac{\omega_s^2}{r},\text{ since } \bar{\omega}_\eta \to \bar{\omega}_\nu}$$
$$-\frac{k_z^2 r}{k_z^2 r^2 + m^2}\frac{\left(2\Omega\bar{\omega}_\eta + \omega_A\omega_c\right)^2}{\omega_A^2 - \bar{\omega}_\nu\bar{\omega}_\eta} + \underbrace{\frac{k_z^2 r^2\left(\bar{\omega}_\eta - \bar{\omega}_\nu\right)}{k_z^2 r^2 + m^2}\frac{\omega_A\omega_c\Omega'}{\omega_A^2 - \bar{\omega}_\nu\bar{\omega}_\eta}}_{=0,\text{ since } \bar{\omega}_\eta \to \bar{\omega}_\nu} \tag{B2}$$

If we then take the final limit $\bar{\omega}_\eta \to \bar{\omega}_\nu \to \bar{\omega}$, we arrive at equation 16 except in r instead of x coordinates, and they converge in a change of coordinates.

$$f = \frac{r\left(\omega_A^2 - \bar{\omega}^2\right)}{k_z^2 r^2 + m^2}, \quad s = 0,$$
$$g = \frac{m}{2}\frac{\mathrm{d}}{\mathrm{dr}}\left\{\frac{\Omega\bar{\omega} + \frac{1}{2}\omega_A\omega_c}{(k_z^2 r^2 + m^2)}\right\} - \frac{\left(\bar{\omega}^2 - \omega_A^2 - \omega_c^2 - \omega_s^2\right)}{r}$$
$$+\frac{1}{4}\frac{k_z^2 r}{k_z^2 r^2 + m^2}\frac{\left(\Omega\bar{\omega} + \frac{1}{2}\omega_A\omega_c\right)^2}{\bar{\omega}^2 - \omega_A^2} \tag{B3}$$